ORIGINAL PAPER

The origin of the carbonate-hosted Huize Zn–Pb–Ag deposit, Yunnan province, SW China: constraints from the trace element and sulfur isotopic compositions of pyrite

Yu-Miao Meng [1] • Rui-Zhong Hu [1,2] • Xiao-Wen Huang [1] • Jian-Feng Gao [1] • Christian Sasseville [3,4]

Abstract

The Huize Zn–Pb–Ag deposit in SW China has an ore reserve in excess of 5 Mt. with an ore grade of ≥25 wt% Zn + Pb and 46–100 g/t Ag. This deposit is hosted in Carboniferous dolostone and limestone. Sulfide mineralization is dominated by sphalerite, galena, and pyrite. Four types of pyrite (Py1 to Py4) are temporally and spatially related to mineralization distinguished on the basis of textural features and mineral associations. Pyrite 1 to 3 corresponds to the pyrite-sphalerite sub-stage, whereas Py4 corresponds to sphalerite-galena-pyrite sub-stage. Pyrite 1 shows zoned texture composed of an inclusion-rich core and an inclusion-free rim, whereas Py2, Py3, and Py4 show replacement relic or overgrowth textures. The zoned texture in Py1 was formed by multiple stages of ore fluids, whereas replacement relic texture in Py2 to Py4 was formed by replacement of pyrite by late Pb-Zn-rich fluids. Trace element variation in pyrite results from a combination of mineral inclusions, co-precipitating minerals, and various fluid compositions. Sphalerite, pyrite, and galena have $\delta^{34}S$ values of 10.4–23.5‰, suggesting that sulfur was probably derived from the thermochemical reduction of marine sulfates. The Huize pyrite has Co and Ni concentrations (0.02–9.5 ppm and 0.08–143 ppm, respectively) and Co/Ni ratios (~0.01–2.63) similar to pyrite from sedimentary exhalative deposits, submarine hydrothermal vents, and sedimentary pyrite, which may be due to pyrite precipitation from low-temperature (<~250 °C), basin brines or seawater. The Co/Ni ratios of the Huize pyrite are lower than those (~0.2–7.2) of pyrite from Mississippi Valley-type Zn-Pb deposits. The Huize pyrite has Co and Ni contents lower than those associated with volcanogenic massive sulfide, iron oxide copper gold, and porphyry Cu deposits, arguing against the involvement of a magmatic/volcanic component and a direct genetic link between Permian Emeishan basalts and Pb-Zn mineralization. Combining with fluid inclusion temperatures and silver grade, we define the Huize deposit as a transitional type between Mississippi Valley-type and high-temperature carbonate-replacement Zn-Pb deposits.

Keywords Trace elements · Sulfur isotopes · Pyrite · LA-ICP-MS · Huize Zn–Pb–Ag · MVT deposits

Introduction

In the western Yangtze Block, SW China, the Sichuan-Yunnan-Guizhou (SYG) Pb-Zn metallogenic belt hosts over 400 Pb-Zn deposits with more than 200 million tons (Mt) of

---

✉ Rui-Zhong Hu
huruizhong@vip.gyig.ac.cn

Extended author information available on the last page of the article

Pb-Zn ores grading 5 wt% Pb and 10 wt% Zn, making it one of the world's largest Pb-Zn producers (Fig. 1) (Liu and Lin 1999; Huang et al. 2003; Hu and Zhou 2012). These deposits are hosted in Sinian (Ediacaran) to Permian carbonate rocks and are controlled by thrust fault-fold structures. Deposits are spatially associated with the ~260 Ma mantle plume-derived Emeishan flood basalts (Fig. 1) (Liu and Lin 1999; Han et al. 2007). The Huize Zn–Pb–Ag deposit is the largest one in the SYG metallogenic belt. Numerous studies of this deposit have been done on the geology (Liu and Lin 1999; Han et al. 2007), geochronology (Zhang et al. 2005a; Li et al. 2007a), and geochemistry (Huang et al. 2001; Zhou et al. 2001; Fu et al. 2003; Han et al. 2004; Zhang et al. 2005b; Li et al. 2006, 2007b). Although the general consensus that the Huize deposit is an example of a Mississippi Valley-type (MVT) Zn-Pb deposit

Fig. 1 **a** A simplified geological map of the South China Block and adjacent regions showing the location of study area (modified from Hu et al. 2017). **b** A map showing the distribution of major Pb-Zn deposits in the Sichuan-Yunan-Guizhou metallogenic belt (modified from Han et al. 2007 and Hu et al. 2017). The large deposit is defined as total Pb and Zn resource higher than 500,000 tons, whereas the small deposit is defined as total Pb and Zn resource lower than 200, 000 tons. The medium deposit is defined as the total Pb and Zn resource between the large and small ones
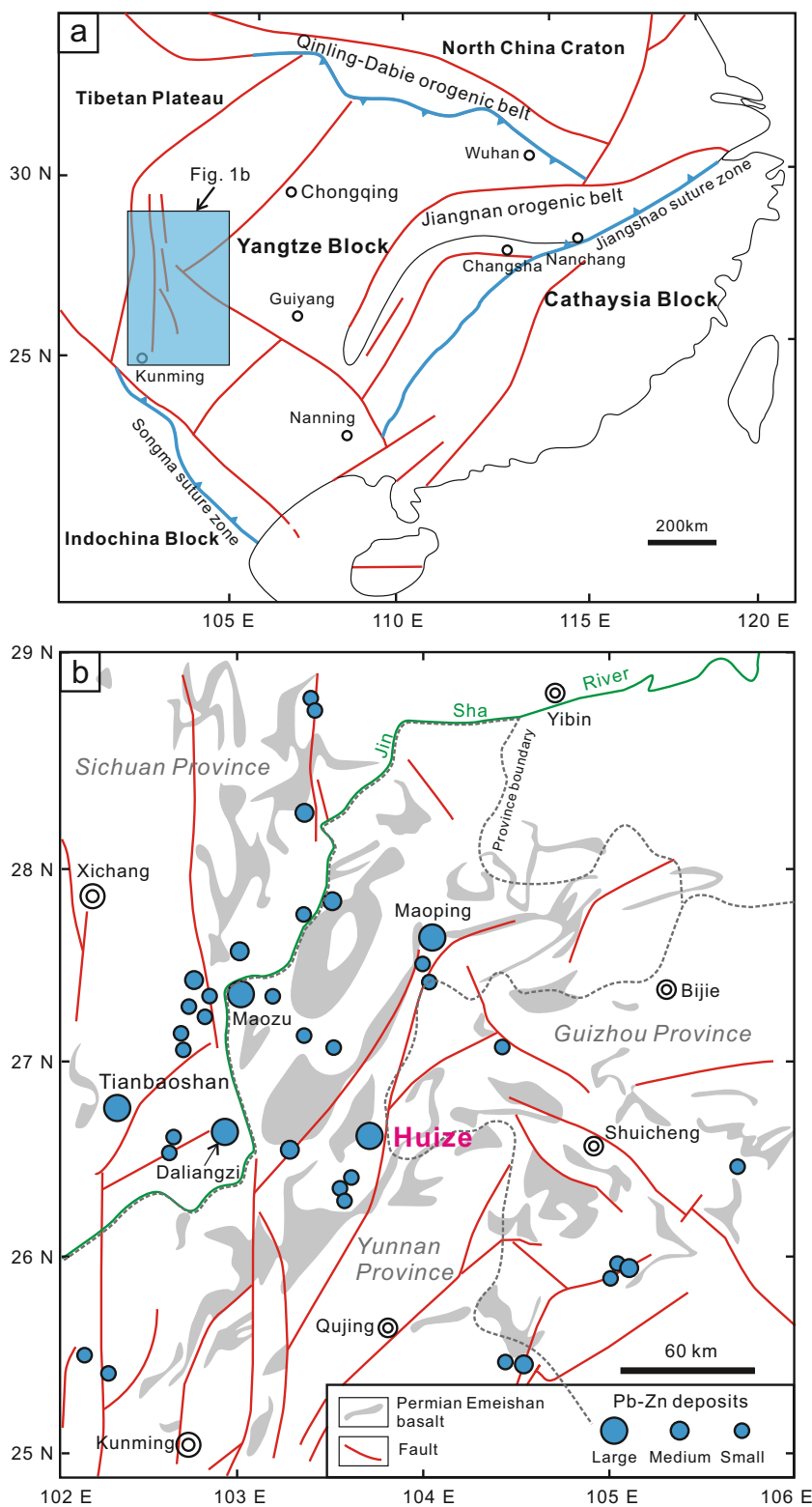
(Zhou et al. 2001; Han et al. 2007; Ye et al. 2011; Hu et al. 2017), the origin of the deposit will be further evaluated here. Mineralization in the Huize deposit is composed dominantly of massive and disseminated sphalerite and galena hosted in carboniferous dolostone and limestone. Pyrite is ubiquitous in

the Huize deposit and constitutes the most abundant sulfide. Petrographic observations have shown multiple generations and types of pyrite with different crystal habits (Huang et al. 2004). Previous studies have focused on the trace element content of pyrite using bulk analytical techniques on

handpicked grains (Huang et al. 2004; Han et al. 2007; Li et al. 2007c), which provided some useful compositional information. However, analysis of pyrite separates suffer from the difficulties in producing pure separates and separating grains of different habits and require in situ trace elemental analysis.

Pyrite can effectively incorporate a wide array of trace metals of economic importance, such as Ag, As, Au, Bi, Cd, Co, Cu, Hg, Mo, Ni, Pb, Pd, Ru, Sb, Se, Sb, Sn, Te, Tl, and Zn, as stoichiometric and non-stoichiometric substitution in the crystal lattice or as nanoparticles or micro-inclusions (Huston et al. 1995; Abraitis et al. 2004; Reich et al. 2005; Large et al. 2009; Deditius et al. 2014; Cook et al. 2016). Pyrite can record changes in fluid chemistry during the evolution of the hydrothermal system from which it was precipitated (Cook et al. 2009; Reich et al. 2013, 2016; Gregory et al. 2016; Tanner et al. 2016) and has been also proposed as a vectoring tool in mineral exploration (Baker et al. 2006; Franchini et al. 2015; Soltani Dehnavi et al. 2015; Mukherjee and Large 2017). Recent studies have demonstrated that the trace element composition of sedimentary pyrite can also serve as a proxy for deep-time ocean-atmosphere evolution (Large et al. 2014, 2017). Pyrite trace element geochemistry has proven useful for understanding the genesis of gold deposits (Large et al. 2009; Deol et al. 2012; Gregory et al. 2016; Tanner et al. 2016), porphyry Cu-Au deposits (e.g., Reich et al. 2013; Zwahlen et al. 2014), volcanogenic massive sulfide (VMS) deposits (Revan et al. 2014; Genna and Gaboury 2015), and sedimentary exhalative (SEDEX) Zn-Pb deposits (Gadd et al. 2016; Mukherjee and Large 2017). Mississippi Valley-type deposits are low-temperature, carbonate-hosted, Zn-Pb ± fluorite ± barite deposits in recognition of the occurrence of many such deposits within the drainage basin of the Mississippi River Valley in the central United States (Leach et al. 2010). Mississippi Valley-type Zn-Pb deposits have fluid compositions and formation conditions different from other types of Zn-Pb deposits that are recorded by trace metal concentrations in pyrite, sphalerite, and galena. In particular, the dissolution-precipitation processes associated with oxidization (sulfate)-reduction (sulfide) is very important for MVT mineralization, which is recorded by pyrite composition/texture and sulfur isotopes.

The aim of this study is to: (1) characterize the textural and compositional styles of pyrite from the Huize Zn–Pb–Ag deposit, (2) discuss the possible factors controlling the trace element distribution in pyrite, and (3) unravel the origin (sulfur and metals) of the Huize Zn–Pb–Ag polymetallic mineralization.

Geological background

Regional geology

The Yangtze Block is separated from the North China Craton by the Triassic Qinling–Dabie orogenic belt to the north and bounded by the Songpan–Ganze Terrane of the Tibetan Plateau to the west (Fig. 1a). To the southeast, the Yangtze Block is separated from the Cathaysia Block by a Neoproterozoic suture zone most likely formed at ~830 Ma (Zhou et al. 2009; Zhao et al. 2011). The Yangtze Block consists of a late Archean basement overlain by a Neoproterozoic to Cenozoic cover. The crystalline basement is represented by a ~2.9 to 3.3 Ga tonalite-trondhjemite-granodiorite (TTG) and metamorphic rocks in the northern part of the Yangtze Block (Qiu et al. 2000; Gao et al. 2011). Paleoproterozoic to Mesoproterozoic strata exposed mainly in the western Yangtze Block are represented by the ~1.7 Ga Dongchuan and ~1.0 Ga Huili Groups (Sun et al. 2009). The cover sequences consist mainly of Paleozoic and Lower Mesozoic strata of shallow marine origin (Zhou et al. 2002; Yan et al. 2003).

In the western Yangtze Block, the ~260 Ma Emeishan Large Igneous Province covers an area of more than 250,000 km^2 (Fig. 1b), which is considered to be the product of a mantle plume (Chung and Jahn 1995; Zhou et al. 2002). This igneous province is dominantly composed of volcanic rocks known as Emeishan flood basalts interlayered with Permian limestone. The province also includes numerous mafic–ultramafic intrusions along major faults, some of which host magmatic sulfide or oxide deposits (Zhou et al. 2008). During the Triassic–Jurassic (~200 Ma), the Yangtze Block collided with the Yidun Arc, resulting in the closure of the Tethys Ocean during the Indosinian Orogeny (Reid et al. 2007).

Over 400 Pb-Zn deposits in the western Yangtze Block are distributed in a large triangular area of 170,000 km^2 at the junction of the Yunnan, Guizhou and Sichuan provinces (Liu and Lin 1999), constituting the SYG Pb-Zn metallogenic belt (Fig. 1b). These Pb-Zn deposits are characterized by irregular ore bodies with simple mineralogy, weak wall rock alteration, and high Zn + Pb grades of ores, and are usually associated with Ag, Ge, Cd, Ga and In mineralization (Liu and Lin 1999). These deposits are hosted in Paleozoic to Mesozoic carbonate rocks, which are overlain by the Permian Emeishan flood basalts (Fig. 1b) (Liu and Lin 1999).

Deposit geology

The Huize deposit is the largest Zn-Pb deposit in the SYG metallogenic belt and includes the Kuangshanchang, Qilingchang (including Dashuijing), and the smaller Yinchangpo sub-districts (Fig. 2) (Han et al. 2007). The Huize deposit has ore reserves in excess of 5 Mt. with an ore grade of ≥25 wt% Zn + Pb (Han et al. 2007). Other economic elements such as Cd (233–488 g/t), Ag (46–100 g/t), and Ge (30–81 g/t) are locally distributed and are also widely extracted (Huang et al. 2004). More than fifty orebodies of various sizes are distributed in the Huize ore district, which includes 42 orebodies in the Kuangshanchang sub-district and 8

orebodies in the Qilingchang sub-district (Han et al. 2007). Among these, the larger No. 1 orebody in the Kuangshanchang sub-district and the larger Nos. 6, 8, and 10 orebodies in the Qilingchang sub-district are most important economically (Fig. 2). Orebodies of the Huize deposit are mainly hosted in the Lower Carboniferous Baizuo Formation, which is composed of grayish-white, yellowish-red, cream-like, and coarse-grained dolostone (Fig. 2). Zinc-Pb ores are highly oxidized in the upper parts, with oxides and sulfides occurring in the middle levels, and sulfide ores in the deeper parts. Sulfide ores are massive and disseminated and are mainly composed of sphalerite, galena, pyrite, calcite, dolomite, and clay minerals (Fig. 3). Light brown through to dark brown sphalerite occurs as massive aggregates or disseminated grains (Fig. 3a-d). Galena mainly occurs as massive aggregates spatially associated with pyrite (Fig. 3e and f) and as disseminations in sphalerite (Fig. 3c and d). Mineral associations show that the Huize deposit was subjected to, from early to late, sedimentary diagenesis, hydrothermal activity, and supergene alteration (Fig. 4) (Han et al. 2007). The hydrothermal mineralization stage can be further divided into pyrite-sphalerite, sphalerite-galena-pyrite, and chalcopyrite-pyrite sub-stages (Fig. 4).

Wall rock alteration includes dolomitization, carbonation, and supergene oxidation (Han et al. 2007). All are closely associated with Pb-Zn mineralization, but only supergene oxidation is a good mineralization indicator. Supergene oxidation occurs as an Fe-capping of Pb-Zn ore.

Methods

Sampling

Twenty-nine pyrite-bearing samples were collected from No. 8 and 10 orebodies in different mining adits at various levels. In situ EPMA and LA-ICP-MS major and trace element analyses were performed on polished thin sections after optical examination using reflected light microscopy to identify the mineralogy and textures of the sulfides, and to avoid possible contamination of mineral inclusions in analyzed pyrite. Most LA-ICP-MS analyses were performed on the EPMA spots. Most sulfide samples for sulfur isotope analysis were separated from the same ores used for polished thin sections studies by a conventional handpicking method, whereas some sulfides were sampled using a micro-drill. Micro-drill sampling was performed before EPMA and LA-ICP-MS analysis on the same thin section.

EPMA analysis

Major and selected trace elements in pyrite were measured using a JEOL JXA-8230 EPMA at the Testing Center of Shandong Bureau of China Metallurgical Geology Bureau, Jinan, China. Elements were analyzed using an accelerating voltage of 15 kV, a beam current of 20 nA, and a beam spot of 1 μm. Matrix effects were corrected using the ZAF software provided by JEOL. Calibration was achieved using a range of
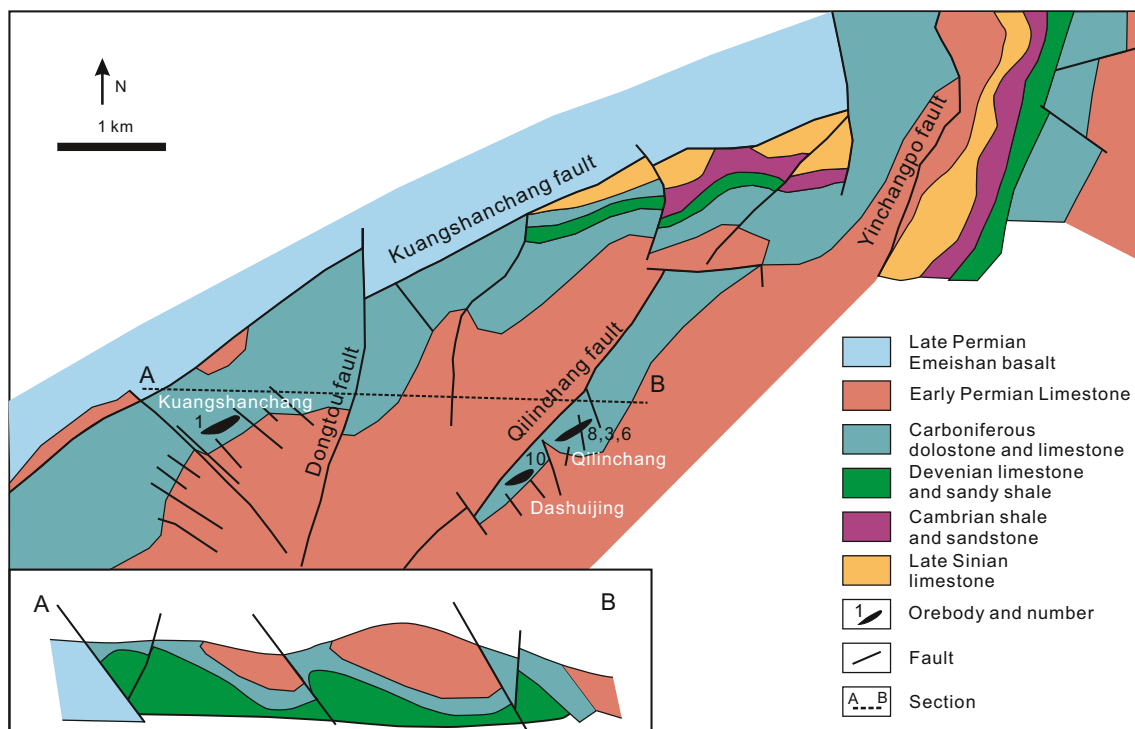
Fig. 2 Simplified geological map of the Huize Zn–Pb–Ag deposit (modified after Han et al. 2007)

Fig. 3 Characteristic photos from typical ores from the Huize Zn–Pb–Ag deposit. **a** Massive ore composed of light brown sphalerite, galena, and calcite. **b** Disseminated ore consisting of sphalerite, galena, and dolomite. **c** Massive ore composed of pyrite, dark brown sphalerite, galena, and calcite. **d** Massive ore composed of light brown sphalerite, pyrite, and minor galena. **e** Massive ore composed of pyrite, sphalerite, galena, and calcite. **f** Massive ore composed of pyrite and galena. The yellow rulers in **a** and **b** are 3 cm long. Abbreviations: *Sp* sphalerite, *Gn* galena, *Py* pyrite, *Cal* calcite, *Dol* dolomite
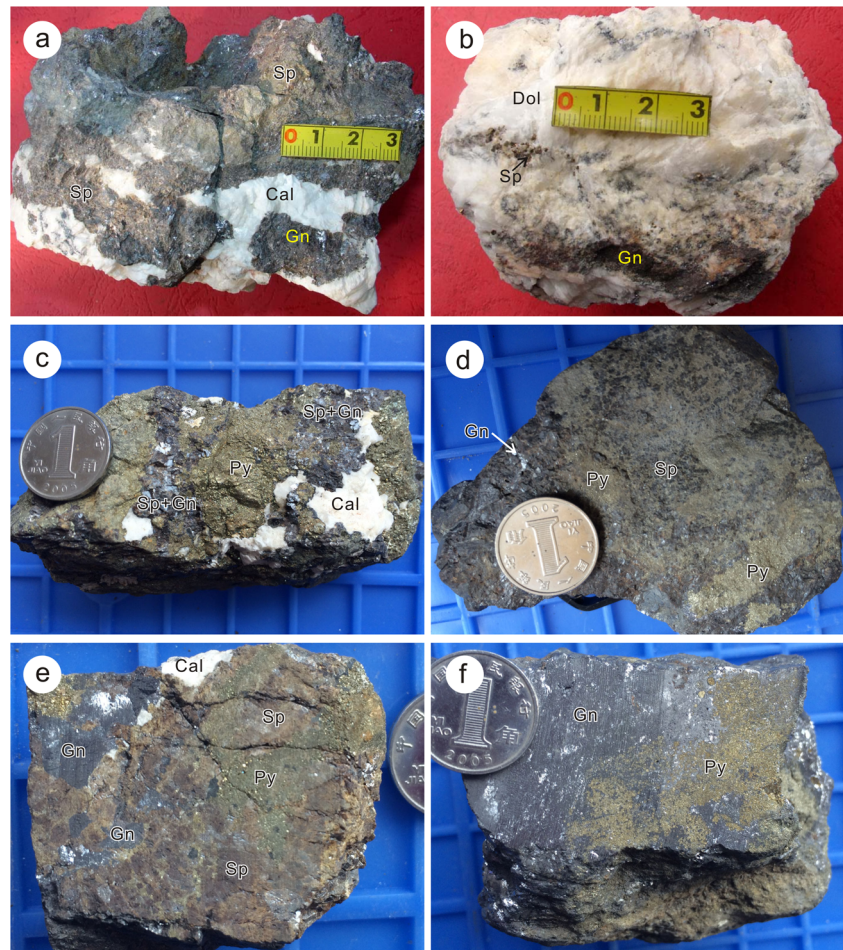
SPI (Structure Probe, Inc., West Chester, PA) metal and mineral standards. The background was measured on one side of the peak for 5–20 s at a position free of interfering element X-ray and the concentration was counted over the peak for 10–40 s depending on the element. The accuracy of the reported values for the analyses is 1–5% depending on the abundance of the element. The detection limits are 36 ppm for S, 77 ppm for Ge and Au, ~90–100 ppm for As, Se, Ag, and Co, ~120–180 ppm for Fe, Ni, Cu, Zn, Cd, Sb, and Pb. In addition to quantitative spot analyses, wavelength dispersive spectrometry (WDS) X-ray maps were collected at an accelerating voltage of 15 kV, a probe current of 100 nA, a point size of 1 × 1 μm, and a dwell time of 3.3 ms for acquisition on each point.

LA-ICP-MS analysis

Twenty-nine elements in 181 grains of pyrite were analyzed with an Agilent 7700x quadrupole ICP-MS coupled to a Photon Machines Excite 193 nm Excimer laser ablation system at the Nanjing Focus Technology Co. Ltd., Nanjing, China. The analytical method is similar to that described by Gao et al. (2015) and Zhang et al. (2016). In order to enhance the sensitivity and lower the instrument background, two routine pumps

were used for the vacuum system. Each analysis was performed by 40 μm diameter ablating spots at 8 Hz with energy of ~5 mJ per pulse for 40 s after measuring the gas blank for 15 s. A total of 34 elements were analyzed: ^{29}Si, ^{31}P, ^{34}S, ^{45}Sc, ^{49}Ti, ^{51}V, ^{52}Cr, ^{55}Mn, ^{57}Fe, ^{59}Co, ^{60}Ni, ^{65}Cu, ^{66}Zn, ^{71}Ga, ^{72}Ge, ^{75}As, ^{77}Se, ^{85}Rb, ^{88}Sr, ^{89}Y, ^{95}Mo, ^{107}Ag, ^{111}Cd, ^{115}In, ^{118}Sn, ^{121}Sb, ^{125}Te, ^{182}W, ^{197}Au, ^{205}Tl, ^{208}Pb, ^{209}Bi, ^{232}Th, and ^{238}U. Off-line selection and integration of background and analyte signals, and time-drift correction and quantitative calibration were performed by the Excel-based Sul cal program (Gao et al. 2015). Sample signal intensity data were converted to concentrations on the basis of calibration against standard analyses of USGS GSE-1G (synthetic basaltic glass) and GSC 12744 (pyrite), and internal normalization to 100% total element abundance (Halicz and Günther 2004). The precision of each analysis is better than 20% for most elements (>1 ppm).

Sulfur isotope analysis

Sulfur isotopes were analyzed by Elemental Analyzer-Isotope Ratio Mass Spectrometer (EA-IRMS), using a Thermo Scientific Flash 2000 high-temperature elemental analyzer coupled to a Thermo Scientific MAT 253 mass spectrometer

at the State Key Laboratory of Ore Deposit Geochemistry, Institute of Geochemistry, Chinese Academy of Sciences, Guiyang, China. Appropriate amounts of powdered sulfide separates were weighed and packed in tinfoil. Sulfur in sulfide minerals was converted to SO_2 for isotopic analysis by burning in the furnace at a temperature of ~1000 °C using a stream of purified oxygen. The sulfur dioxide was then carried by helium into the mass spectrometer. The sulfur isotopic compositions are expressed using the delta per mil notation ($\delta^{34}S$) with respect to Vienna Canyon Diablo Troilite (VCDT).

Results

Petrography

Reflected light microscopy and EPMA reveal multiple types and generations of pyrite in the Huize deposit. According to the mineral associations and crystal habits of pyrite, samples in this study are divided into four types that are defined as Py1, Py2, Py3, and Py4 from early to late. Pyrite 1, Py2, and Py3 correspond to the pyrite-sphalerite sub-stage (Fig. 4). These three pyrite types are associated with an increasing proportion of sphalerite. Py4 corresponds to sphalerite-galena-pyrite sub-stage (Fig. 4). Pre-ore sedimentary/diagenetic pyrite and pyrite from pyrite-chalcopyrite sub-stage are absent in this study.

Samples containing Py1 are disseminated ores and mainly composed of pyrite and dolomite along with minor sphalerite and galena (Fig. 5a and b). Sphalerite is anhedral and is

disseminated in dolomite, whereas galena grows along pyrite fractures and grain boundaries. Pyrite 1 is euhedral and is about 50–100 μm in diameter. Some pyrite grains show zoned textures composed of an inclusion-rich core and an inclusion-free rim (Fig. 6a).

Ores containing Py2 are commonly disseminated and composed of main pyrite (~30 modal%) and dolomite (~65 modal%) and minor sphalerite and galena (~5 modal%). Pyrite 2 is coarse-grained (> 1 mm) (Fig. 5c) and occurs as pentagonal dodecahedron crystals that are locally fractured (Fig. 5c). No major element zonation was observed in Py2 using back-scattered electron imaging (Fig. 5d). Ore containing Py3 is composed of ~80 modal% sphalerite and ~20 modal% pyrite (Fig. 5e), forming a network structure. Only minor galena grows along the spaces between pyrite grains (Fig. 5f). Pyrite 3 is mainly rounded and fine-grained (50–100 μm).

Ores containing Py4 are mainly massive and composed of varying amounts of pyrite, sphalerite, and galena (Fig. 5g and h). Pyrite 4 commonly has obvious replacement or over-growth textures (Figs. 5, 6b-d, 7). Euhedral pyrite was replaced by sphalerite and galena to form subhedral to anhedral relics (Fig. 5g) or zoned pyrite (Figs. 6b–f and 7a, b). Late recrystallized pyrite also grows along the margin of early pyrite, forming different generations of pyrite (Fig. 6d).

EPMA results

In order to investigate the chemical variation of different pyrite domains, EPMA spot analyses were carried out on

Fig. 5 Photomicrographs of selected ores showing textures of different types of pyrite. Images in the left are acquired under reflected light, whereas those in the right are back-scattered electron images. a and b Cubic pyrite disseminated in dolomite. Sphalerite occurs as anhedral crystal disseminated in dolomite, whereas galena occurs as veins filling in fractures of pyrite or grows along pyrite grain boundaries. Pyrite grains are composed of an inclusion-rich core and an inclusion-free rim and are crosscut by galena veins. c and d Sub-millimeter pyrite (up to 1 mm) disseminated in dolomite exhibiting fractured pentagonal dodecahedron crystal habit. e and f Subhedral pyrite growing within sphalerite intergrain space. Galena grows along pyrite grain boundaries or occurs within sphalerite grains. g and h Anhedral to subhedral and inclusion-rich pyrite replaced by sphalerite and galena, forming the metasomatic relic texture. Abbreviations: Py pyrite, Sp sphalerite, Gn galena, Dol dolomite, Cal calcite
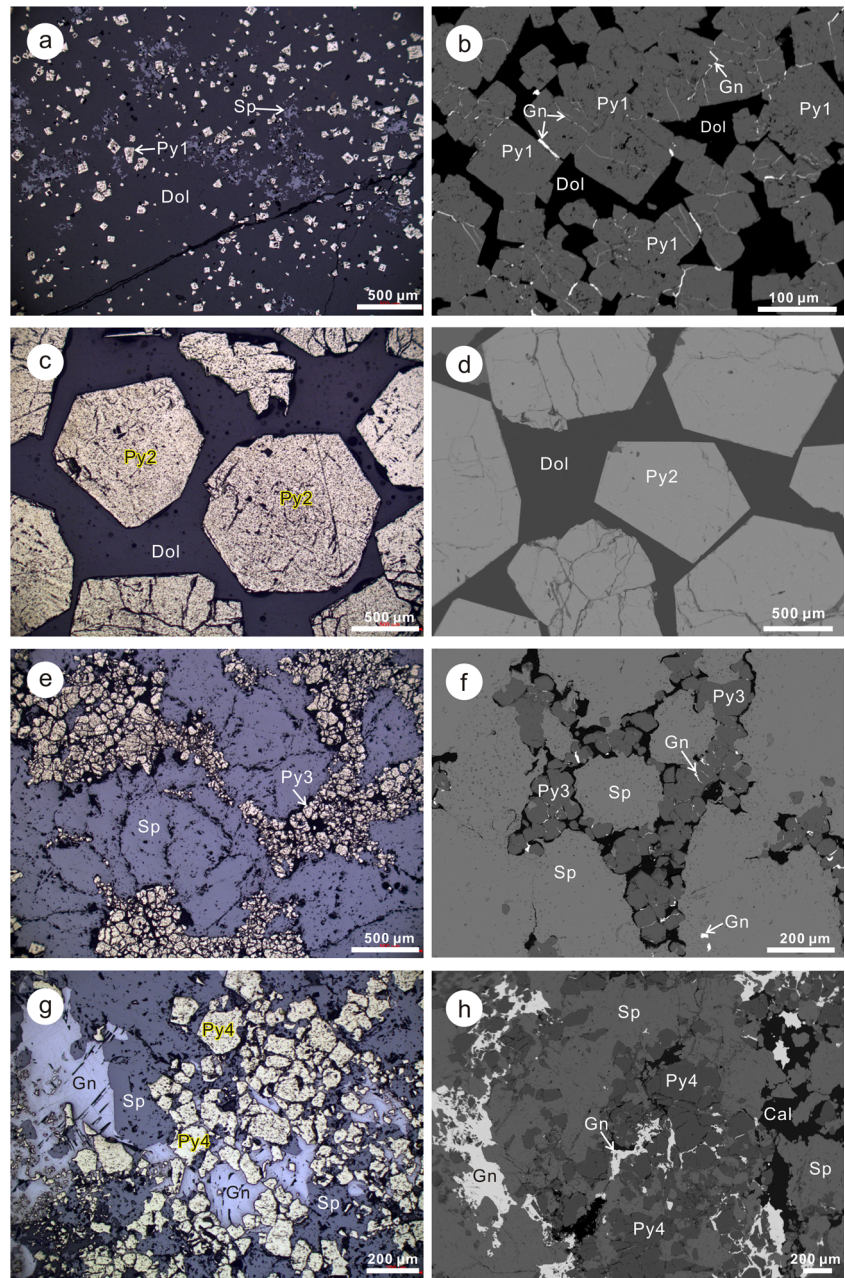
single pyrite grains. Laser ablation ICP-MS analyses were not obtained because most of the pyrite domains in Py1 and Py4 were smaller than the diameter of the ablation crater (i.e., 40 μm). Back-scattered electron images and related EPMA results of pyrite are shown in Fig. 6. For sample LC-1 (Py1), the inclusion-rich core generally has lower Co, Pb, Zn, and higher Au, Se, and Ge contents than the inclusion-free rim (Fig. 6a). Nickel, Sb, and Cd show no systematic variations because most of them have concentrations below detection limits. For sample LHZ-117 (Py4), the Co, Pb, Zn, and Cd contents decrease from the core to the middle and then to the rim, whereas Sb and As contents increase (Fig. 6b). The core of sample LHZ-120 (Py4), contains higher Co and Pb contents but lower As, Cu, and Se contents than the rim (Fig. 6c). The recrystallized margin of pyrite sample LHZ-67 (Py4) has higher As, Ni, Cu, and Ag contents but lower Cd contents than the interior (Fig. 6d). Arsenic is enriched in the core of sample HZ14–5 (Py4), whereas Pb and Sb are concentrated in the rim (Fig. 6e). Sample MYMHZ-31 (Py4) has similar core-rim texture to sample HZ14–5 but has different trace element patterns with the enrichment of Cu, Se, Cd, and Zn in the core and Au in the rim (Fig. 6f). Lead contents are similar between core and rim, whereas As, Co, and Ag contents are different but lack systematic variation (Fig. 6f).
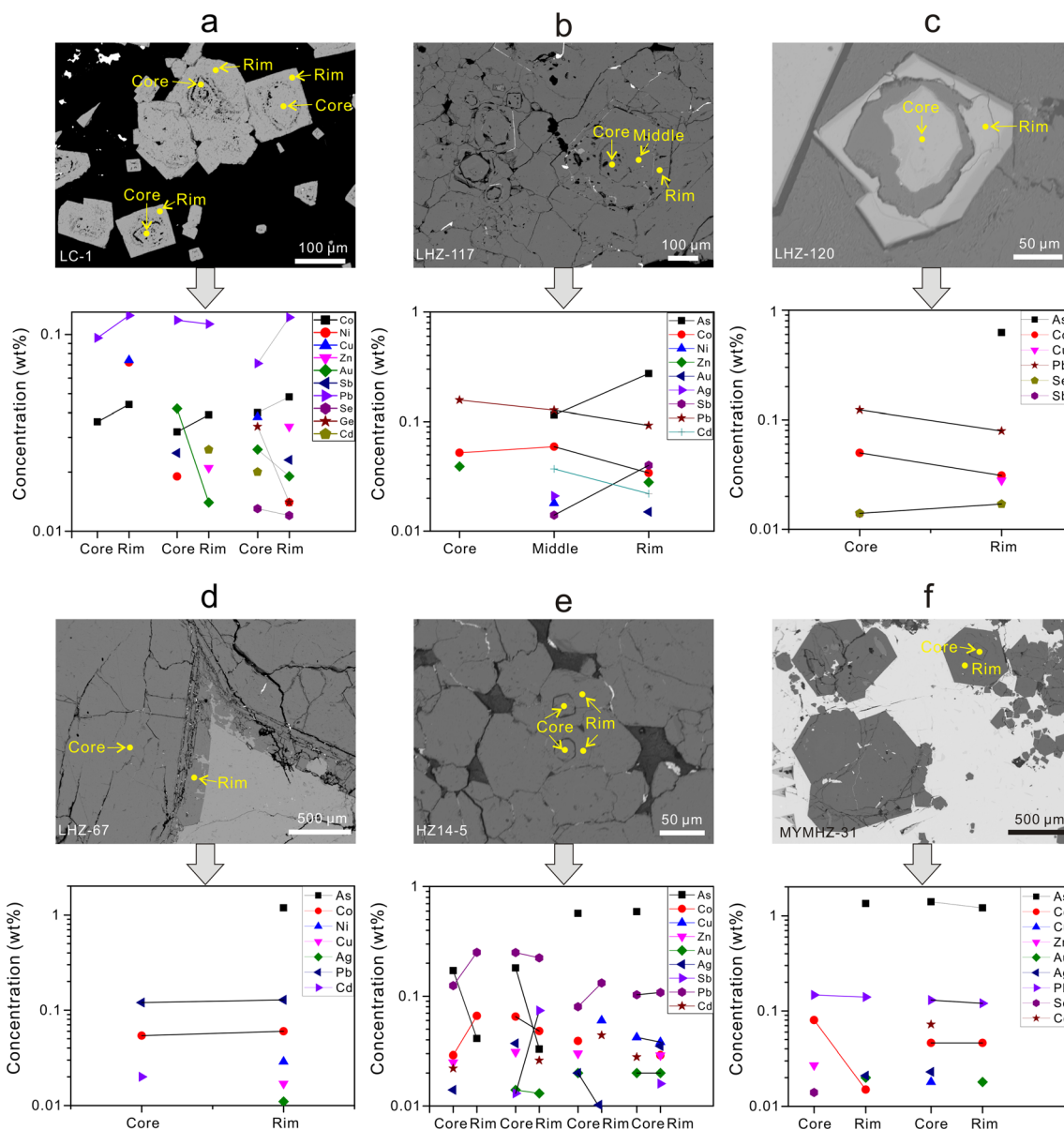
Fig. 6 Compositional variations of different pyrite domains, based on EPMA data. **a** Pyrite composed of an inclusion-rich core and an inclusion-free rim (sample LC-1). **b** Pyrite composed of core, middle, and rim domains (sample LHZ-117). **c** Pyrite composed of core and rim (sample LHZ-120). **d** Pyrite composed of primary core and overgrowth margin (sample LHZ-67). **e** and **f** Pyrite composed of core and rim domains

Electron microprobe BSE and element maps show that pyrite sample LHZ-67 (Py4) with replacement relic texture (pyrite was replaced by sphalerite and galena) has variable As contents (Fig. 7a). The variable Pb and Zn contents in pyrite are due to the small sphalerite and galena inclusions (Fig. 7a). The coupled Pb and Cd mapping indicates that Cd is more enriched in galena than pyrite (Fig. 7a). Another pyrite sample LHZ-117 (Py4) also shows various As contents (Fig. 7b). The chemical zoning of Zn (Fig. 7b) indicates minor sphalerite in the fractures of pyrite, whereas the Pb anomaly in pyrite (Fig. 7b) is due to galena inclusion.

LA-ICP-MS results

The trace element contents of Py1 ($n = 10$), Py2 ($n = 20$), Py3 ($n = 39$), and Py4 ($n = 211$) were determined by LA-ICP-MS. A total of 34 elements were determined, of which Se, Ga, Sc, Rb, Sr, Y, Mo, Cd, In, Sn, W, Au, and Tl were below the detection limits. Only Ti, V, Cr, Mn, Co, Ni, Cu, Zn, Ge, As, Ag, Sb, Te, and Pb can be used to investigate the pyrite chemistry. Full spot analytical results of pyrite from the Huize deposit are given in Online Resource 1. The average values and standard deviations of trace element contents in pyrite are
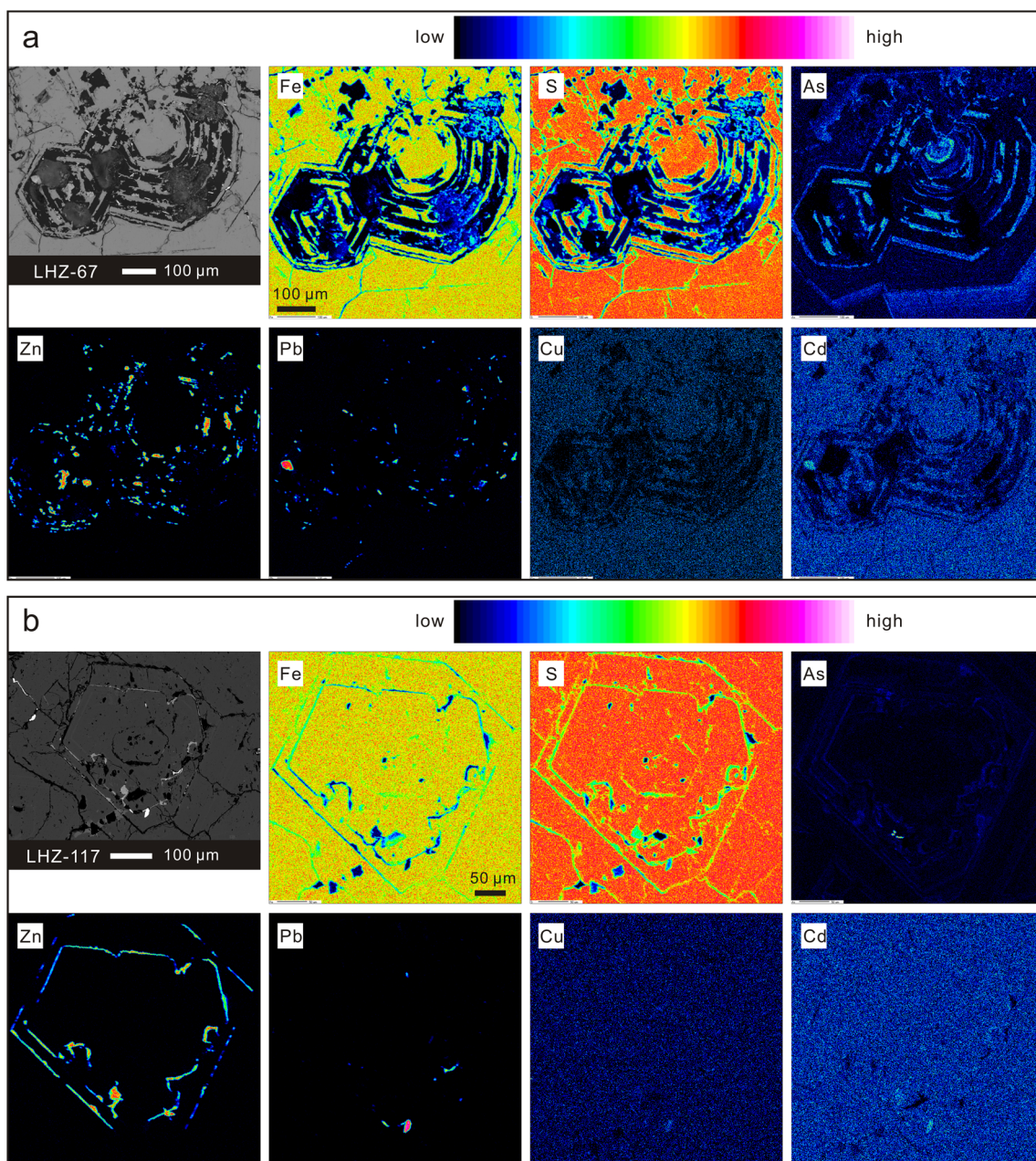
Fig. 7 Back-scattered electron microphotographs of pyrite and the wavelength dispersive X-ray elemental maps. **a** Pyrite replaced by sphalerite and galena to form replacement relic texture (sample LHZ-67). **b** Pyrite replaced by sphalerite to form zoned texture (sample LHZ-117)

listed in Table 1. In general, pyrite has various trace element contents that span five orders of magnitude (Fig. 8). Pyrite has V, Mn, Co, Ge, and Ti contents lower than ~10 ppm, Ti, Cr, Zn, and Ag contents lower than ~100 ppm, Ni and Cu contents up to ~140 ppm, Sb content up to ~380 ppm, Pb content up to ~1600 ppm, and As content up to ~16,000 ppm.

The trace element concentrations vary between the pyrite types (Figs. 8 and 9). Pyrite 1 has the highest Cr, Ni, Zn, Pb, and Ag contents, whereas Py2 has the highest Cu and As contents but the lowest amounts of Zn (Fig. 8). Pyrite 3 and Py4 have similar Mn, Cu, As, Ag, Sb, and Pb

contents, but the former has lower Ti, V, Cr, Ge, and Te contents and higher Co, Ni, and Zn contents than the later (Fig. 8). There is a positive correlation between Co and Ni for Py3 with a correlation coefficient (R^2) of 0.90, whereas weak correlations between these elements are observed for Py1, Py2, and Py4 ($R^2 = 0.19$, 0.10, and 0.34) (Fig. 9a). Pyrite 1 has a constant Co/Ni ratio of ~0.01, whereas Py2 and Py3 show limited variations of Co and Ni content with Co/Ni ratios ranging from 0.1 to 1 (Fig. 9a). Pyrite 4 has more variable Co and Ni contents with Co/Ni ratios ranging from 0.01 to 1 (Fig. 9a). Weak

Table 1 LA-ICP-MS trace element composition (in ppm) of pyrite from the Huize deposit

Sample no. Pyrite type	DL	LC1-1 Py1		LHZ-116 Py2		LHZ-119 Py2		HZ14-54 Py3		HZ14-27 Py3		HZ14-49 Py3		LHZ-43 Py3	
		ave (n=10)	stdev	ave (n=10)	stdev	ave (n=10)	stdev	ave (n=9)	stdev	ave (n=10)	stdev	ave (n=10)	stdev	ave (n=10)	stdev
Ti	0.89	13.79	0.7	14.3	0.81	12.23	2.83	8.11	0.76	7.42	0.75	11.74	10.57	6.84	0.51
V	0.07	0.17	0.04	0.08	0.01	0.79	1.19	0.09	0.01	0.11	0.01	0.17	0.06	0.08	
Cr	1.17	32.01	12.13	3.24	1.8	7.05	3.08	3.17	1.2	2.7	1.38	2.36	0.83	2.37	0.73
Mn	0.19	1.26	1.56	0.54	0.27	0.74	0.22			1.43	2.19	0.25	0.02		
Co	0.02	0.69	0.35	0.27	0.28	0.27	0.14	0.53	0.94	0.1	0.02	1.34	1.85		
Ni	0.07	60.48	38.25	1.28	0.98	1.2	0.89	2.69	3.55	0.66	0.72	11.77	21.86	1.36	2.3
Cu	0.07	25.17	22.75	34.56	41.55	46.09	25.36	5.91	3.65	1.36	1.4	9.43	11.44	0.31	0.26
Zn	0.69	24.11	29.49	1.24	0.28	1.69	0.87	1.02	0.34	0.9	0.15	1.99	0.96	1.71	1.69
Ge	0.38	4.28	0.3	4.4	0.34	2.93	0.21	1.9	0.18	1.81	0.18	1.81	0.24	1.76	0.16
As	0.93	131	23	5270	5434	8550	3141	835	961	846	433	2704	1451	117	85
Ag	0.02	8.58	6.72	1.34	1.07	2.3	2.34	1.41	1.15	0.55	0.36	2	2.61	1.29	1.56
Sb	0.04	8.55	5.29	8.6	8.36	7.53	7.47	77.93	70.59	5.55	4.26	60.59	103.14	4.43	4.76
Te	0.01	0.41	0.33	0.3	0.11	0.53	0.43	0.09	0.03	0.08	0.02	0.13	0.07	0.04	0
Pb	0.02	290	242	32	46	44	67	344	317	24	35	296	354	20	26

Sample no. Pyrite type	HZ14-5 Py4		HZ14-21 Py4		LHZ-117 Py4		LHZ-110 Py4		LHZ-120–1 Py4		LHZ-125 Py4		LHZ-126 Py4	
	ave (n=10)	stdev	ave (n=10)	stdev	ave (n=10)	stdev	ave (n=9)	n=9	ave (n=9)	stdev	ave (n=10)	stdev	ave (n=15)	stdev
Ti	23.99	7.99	15.43	0.8	32.42	3.94	11.39	1.79	12.85	7.3	10.26	0.81	22.54	13.35
V	0.15	0.1	0.46	0.22	0.19	0.06	0.1	0.02	0.09	0.01	0.12	0.03	0.13	0.03
Cr	5.84	4.49	12.17	6.15	2.54	0.88	8.23	4.61	4.32	2.74	6.83	6.09	7.17	4.81
Mn	0.4	0.16	0.81	0.69	1.79	3.41	1.53	1.64	0.52	0.17	0.44	0.16	0.37	0.09
Co	0.16	0.1			0.04	0	0.47	0.71	1.13	2.47	0.26	0.2	0.08	0.06
Ni	1.73	1.45	1.7	1.43	1.09	0.86	0.97	0.69	3.91	7.11	1.03	1.46	0.79	0.63
Cu	2.38	1.85	11.5	10.93	6.55	4.05	3.38	3.81	6.85	14.73	8.61	5.39	2.01	1.88
Zn	1.49	0.5	2.09	0.85	1.68	1.36	1.45	0.52	0.86	0.18	1.33	0.62	1.42	0.58
Ge	4.52	0.5	4.62	0.21	4.05	0.39	3.1	0.27	3	0.3	3.14	0.34	3.69	0.37
As	1285	982	568	519	1526	1000	744	824	1865	2525	2658	1358	694	508
Ag	4.08	7.62	7.29	6.73	1.2	1.6	0.45	0.45	1.08	1.29	1.44	1.72	0.82	0.8
Sb	61.57	74.14	39.1	33.96	24.82	39.06	16.87	15.7	9.58	13	8.08	7.62	10.85	14.35
Te	0.33	0.25	0.17	0.11	0.45	0.41	0.5	0.37	0.45	0.31	0.68	0.34	0.74	0.4
Pb	212	304	580	708	114	181	94	101	61	80	69	97	70	100

Table 1 (continued)

Sample no.	MYMHZ-36 Py4		MYMHZ-31 Py4		MYMHZ-40 Py4		MYMHZ-12 Py4		LHZ-67 Py4		LHZ-8 Py4		LHZ-23 Py4		LHZ-14 Py4	
Pyrite type	ave (n=10)	stdev	ave (n=8)	stdev	ave (n=10)	stdev	ave (n=9)	stdev	ave (n=10)	stdev	ave (n=10)	stdev	ave (n=8)	stdev	ave (n=7)	stdev
Ti	22.75	2.08	21.7	10.44	13.08	0.71	14.58	6.56	11.45	0.73	9.64	1.52	10.11	0.75	9.56	0.39
V	0.2	0.07	0.35	0.31	0.24	0.24	0.26	0.1	0.25	0.23	0.14	0.04	0.1		0.1	0.01
Cr	8.51	3.38	2.03	0.8	3.14	1.18	4.69	1.69	8.38	4.2	7.75	4.82	5.54	2.67	3.22	1.4
Mn	0.97	0.33	0.52	0.23	0.24		1.64	1.34	0.33	0.09	0.43	0.09	1.75	2.35	0.47	0.18
Co			0.64	0.53	0.08	0.04	0.31	0.22	0.17	0.16	0.22	0.29	0.13	0.1	0.05	0
Ni	0.8	0.34	1.85	1.16	1.15	0.8	6.27	4.52	1.02	1.16	1.76	1.14	1.27	1.37	0.92	1.18
Cu	1.54	1.23	42.87	29.21	1.48	0.65	1.33	0.62	2.09	1.42	1.67	0.85	1.24	1.29	1.84	1.54
Zn	1.86	0.74	1.29	0.46	3.55	7.16	2.51	1.2	1.42	0.53	1.93	0.53	2.32	1.3	1.56	1.03
Ge	3.42	0.35	2.83	0.28	3.03	0.34	3.22	1.12	2.87	0.33	2.73	0.38	2.66	0.41	2.86	0.18
As	1526	2496	8312	4204	52	118	232	114	341	310	96	114	647	321	94	80
Ag	0.9	0.81	6.75	10.54	1.49	0.94	0.71	0.38	1.7	1.87	0.47	0.32	0.14	0.13	2.13	1.95
Sb	61.87	79.6	28.91	28.9	5.93	7	32.22	52.45	5.78	13.69	205.79	92.5	3.75	3.21	14.69	14.34
Te	0.47	0.35	0.89	0.53	0.42	0.39	5.63	3.58	0.83	0.33	1.03	0.23	0.63	0.34	0.37	0.28
Pb	193	223	201	261	47	69	192	167	34	68	659	269	30	269	67	83

Sample no.	HZ-42 Py4		HZ14-51 Py4		MYMHZ14-51 Py4		HZ14-34 Py4		FSLHZ-04 Py4		MYMHZ-45 Py4		MYMHZ-32 Py4	
Pyrite type	ave (n=10)	stdev	ave (n=9)	stdev	ave (n=10)	stdev	ave (n=10)	stdev	ave (n=10)	stdev	ave (n=9)	stdev	ave (n=8)	stdev
Ti	19.84	1.15	67.86	24	30.7	16.22	14.61	0.82	13.06	1.14	11.34	1.13	9.64	0.82
V	0.17	0.08	0.61	0.53	0.11	0.03	0.16	0.06			0.14	0.07	0.17	0.07
Cr	2.99	1.09	4.04	1.99	5.46	2.93	10.93	11.18	2.78	1.47	4.82	2.94	6.09	3.17
Mn	0.83	1.21	0.33	0.1	0.41	0.05	0.44	0.17	0.41	0.27	0.26	0.03	0.26	
Co			0.16	0.11	1.37	2.86	0.46	0.64					0.11	0.09
Ni	0.42	0.37	1.05	0.59	2.12	3.54	6.39	7.53	0.18	0.07	0.14	0.02	0.7	0.63
Cu	17.74	17.69	3.11	2.78	2.86	3.91	2.33	2.85	2.77	2.05	1.08	0.76	1.14	1.27
Zn	1.12	0.3	1.32	0.39	1.02	0.2	2.93	1.87	1.21	0.27	1.87	1.44	2.93	2.33
Ge	2.75	0.23	2.75	0.21	2.55	0.12	2.41	0.08	2.32	0.21	2.5	0.17	2.24	0.15
As	7330	5231	976	862	10	14	1465	1796	604	222	25	23	96	131
Ag	3.57	3.21	0.68	0.8	0.11		0.58	0.88	0.83	1.38	0.13	0.07	1.36	1.88
Sb	45.48	20.96	17.61	9.54	0.6	0.66	5.3	6.78	5.43	13.24	14.11	15.67	7.15	8.19
Te	0.33	0.1	0.34	0.11	0.17	0.07	0.22	0.1	0.31	0.12	0.17	0.02	0.14	0.12
Pb	573	311	98	144	5	12	21	25	11	28	46	51	45	51

Numbers in parenthesis represent the number of analyzed spots. *DL* detection limit, *ave* average, *stdev* standard deviation

Fig. 8 Box and whisker plot of trace element concentrations with respect to pyrite types. Boxes outline the 25th to 75th percentiles and whiskers extend to the minimum and maximum values. The short line in the box represents the median value, whereas the circle filled white represents the mean value. Trace element contents below the limit of detection were removed from the box and whisker plot
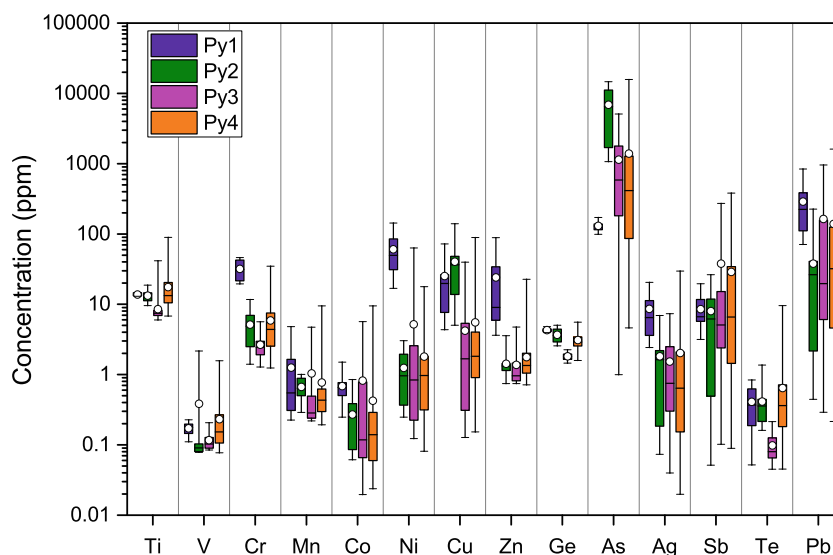
correlations between As and Cu are observed for Py1, Py2, and Py3 ($R^2 = 0.46$, 0.47, and 0.43), whereas As shows a positive correlation with Cu for Py4 ($R^2 = 0.66$) (Fig. 9b). It is worth noting that As in Py3 and Py4 shows a better positive correlation with Cu only when As contents are higher than ~200 ppm (Fig. 9b). Lead shows a positive correlation with Ag for all pyrite types except Py4 (Fig. 9c). The correlation coefficients between Pb and Ag are 0.84, 0.60, 0.83, and 0.16 for Py1 to Py4, respectively. There is a positive correlation between Pb and Sb for all pyrite types except Py1, with R^2 of 0.08, 0.56, 0.70, and 0.57 for Py1 to Py4, respectively (Fig. 9d). Due to different As and Ge contents, different types of pyrite define their own fields (Fig. 9e). Pyrite 1 and Py3 are distinguished from each other based on different Ge, Ni, Ti, and Cr contents (Fig. 9f-h). Pyrite 4 has more variable compositions and commonly overlaps those of Py2 (Fig. 9f-h).

Sulfur isotope composition of sulfides

Sphalerite, pyrite, and galena are characterized by heavy sulfur isotope with $\delta^{34}S_{VCDT}$ values ranging from 10.4 to 23.5‰ with a peak of 14–16‰ (Table 2, Fig. 10). Sphalerite has $\delta^{34}S_{VCDT}$ values ranging from 12.2 to 24.5‰, whereas pyrite and galena show relatively limited variations in sulfur isotope compositions with $\delta^{34}S_{VCDT}$ values ranging from 14 to 18‰ and 10 to 12‰, respectively (Fig. 10). For sulfides from the same ore, sulfur isotope composition follows the trend of $\delta^{34}S_{pyrite} > \delta^{34}S_{sphalerite} > \delta^{34}S_{galena}$ (Table 2), which is consistent with isotopic equilibrium. Different types of pyrite show no obvious differences in sulfur isotope composition. Pyrite 3 has $\delta^{34}S_{VCDT}$ values ranging from 13.8 to 14.9‰ (n = 3), whereas Py4 has $\delta^{34}S_{VCDT}$ values ranging from 13.2 to 17.1‰ (n = 23) (Table 2).

Discussion

The formation of pyrite with different textures

The three main textures in Huize pyrite are zoning (Py1), replacement relics (Py4), and overgrowths on Py4 (Fig. 6). Zoned pyrite is composed of an inclusion-rich core and an inclusion-poor rim (Fig. 6a), similar to zoned pyrite in gold deposits elsewhere (Baker et al. 2006; Large et al. 2009; Tanner et al. 2016). The inclusion-rich cores have slightly higher Au but lower As and Co contents than inclusion-poor rims (Fig. 6a). The formation of zoned pyrite may be related to the mixing of hydrothermal fluids of different compositions or dissolution-reprecipitation of pyrite under kinetically favorable conditions (Deditius et al. 2011; Pačevski et al. 2012). Pyrite 4 was replaced by sphalerite and galena because of large amounts of microinclusions of sphalerite and galena in pyrite (Fig. 7a and b). Some relic pyrite grains also formed as a result of the replacement by calcite or dolomite (Fig. 6c). The limited variations of trace elements in pyrite with replacement relic texture indicate that later hydrothermal fluids responsible for sphalerite and galena formation did not significantly change the composition of precursor pyrite. Alternatively, the subtle compositional variation in pyrite is most likely due to the fluctuating physicochemical conditions such as temperature and pressure during the growth of pyrite (Deditius et al. 2014). Primary pyrite and pyrite overgrowths have similar Pb and Co contents (Fig. 6d).

Controls on the trace element variations in pyrite

Variations in trace elements of pyrite can be attributed to mineral inclusions (sulfides, silicates, and carbonates), coprecipitated minerals, and variable fluid composition, and physicochemical conditions of ore-forming fluids such as

Fig. 9 Binary plots of selected trace elements in pyrite. **a** Plot of Co vs. Ni for different pyrite types. Correlation coefficients (R^2) between Co and Ni for Py1 to Py4 are 0.19, 0.10, 0.90, and 0.34, respectively. **b** Plot of Cu vs. As. Stronger positive correlation between Cu and As for analyses when As contents are higher than ~200 ppm. Correlation coefficients between Cu and As for Py1 to Py4 are 0.46, 0.47, 0.43, and 0.66, respectively. **c** Positive correlation between Pb and Ag for Py1 to Py4 with correlation coefficients of 0.84, 0.60, 0.83, and 0.16, respectively. **d** Plot of Pb vs. Sb for different pyrite types. Correlation coefficients between these elements are 0.08, 0.56, 0.70, and 0.57 for Py1 to Py4. **e-g** Plots of Ge versus As, Ni, and Ti. **h** Plot of Ti vs. Cr showing different compositional populations of pyrite types
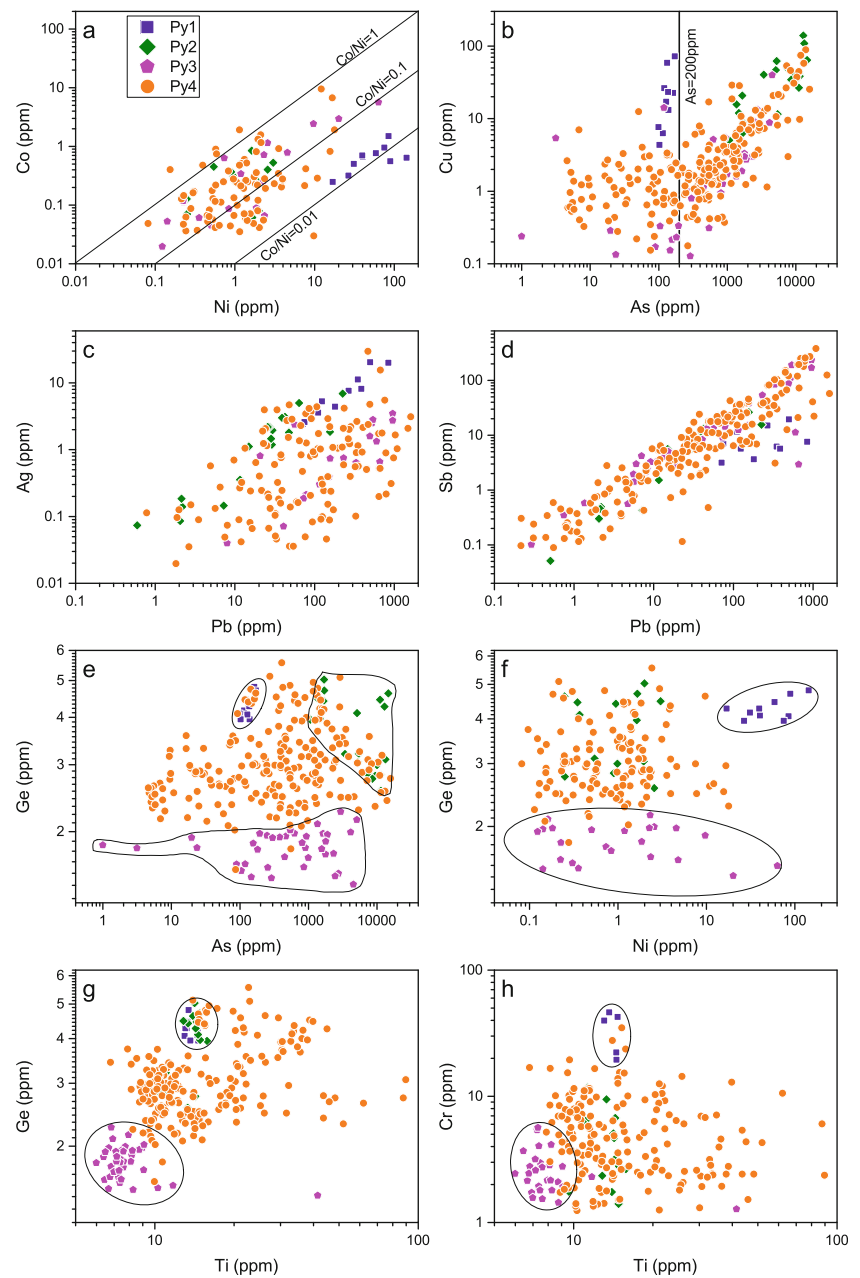
temperature, sulfur fugacity, and pH (Reich et al. 2013; Wohlgemuth-Ueberwasser et al. 2015). George et al. (2016) showed that elements Mn, Fe, Co, Cu, Zn, Ga, As, Se, Ag, Cd, In, Sb, Te, Tl and Bi in co-crystallized sphalerite–galena–chalcopyrite are mainly controlled by element oxidation state, ionic radius of the substituting element, element availability and the maximum trace element budget that a given sulfide mineral can accommodate. Temperature, pressure, redox conditions and metal source, do not generally appear to influence the preferred partitioning of all the trace elements in base metal sulfides (George et al. 2016). Here, the main factors controlling the trace element variations in pyrite from the Huize deposit are discussed.

Sulfide mineral inclusions such as sphalerite, chalcopyrite, and galena are common in pyrite from the Huize deposit. Sulfide inclusions can be identified by abrupt increases and then decreases in the ablation count–time profiles (Online Resource 2). The effect of mineral inclusions on trace element composition of pyrite can be eliminated by scrutinizing the LA-ICP-MS element profile to see whether one element suddenly increases along with another element when a possible inclusion is hit.

Because a lot of LA-ICP-MS data are below detection limits, these censored data cannot be used for box and binary plots and some of useful information about pyrite chemistry may be lost. In order to better understand the occurrences of

Table 2 Sulfur isotope composition of sulfides from the Huize deposit

Sample no.	Mineral	δ^{34}S (‰)	References	Sample no.	Mineral	δ^{34}S (‰)	References
LHZ-117	Py4	16.7	This study	HQ-491	Gn	14.8	Han et al. (2007)
LHZ-67	Py4	14.2	This study	HQ-495	Gn	10.9	Han et al. (2007)
LHZ-8	Py4	16.3	This study	HQ-490	Py	15.1	Han et al. (2007)
LHZ-23	Py4	15.6	This study	HQ-493X	Py	14.2	Han et al. (2007)
LHZ-14	Py4	15.0	This study	HQ-495	Py	15.3	Han et al. (2007)
LHZ-43	Py3	14.9	This study	HQ-487	Sp	23.5	Han et al. (2007)
HZ14–5	Py4	16.8	This study	HQ-491	Sp	14.9	Han et al. (2007)
HZ14–34	Py4	14.4	This study	HQ-495	Sp	12.7	Han et al. (2007)
HZ14–27	Py3	14.9	This study	HQ-498	Sp	13.4	Han et al. (2007)
HZ14–42	Py4	14.4	This study	15.00	Gn	11.3	Li et al. (2007b)
HZ14–49	Py3	13.8	This study	8--1	Gn	14.5	Li et al. (2007b)
HZ14–51	Py4	17.1	This study	H10–22-2	Gn	13.5	Li et al. (2007b)
MYMHZ-31	Py4	15.0	This study	H10–3-2	Gn	14.4	Li et al. (2007b)
MYMHZ-40	Py4	13.5	This study	H10–18	Py	15.7	Li et al. (2007b)
MYMHZ-12	Py4	15.9	This study	H10–20-5	Py	16.5	Li et al. (2007b)
MYMHZ-45	Py4	14.6	This study	H10–3-3	Py	17.4	Li et al. (2007b)
MYMHZ-32	Py4	15.3	This study	HQ-485	Py	14.4	Li et al. (2007b)
FSHZ-04	Py4	16.9	This study	HQ-486	Py	14.9	Li et al. (2007b)
MYMHZ-12*	Py4	14.8	This study	HQ-487	Py	15.8	Li et al. (2007b)
MYMHZ-24*	Py4	13.9	This study	HQ-488	Py	16.2	Li et al. (2007b)
MYMHZ-36*	Py4	14.1	This study	HQ-489	Py	16.4	Li et al. (2007b)
MYMHZ-40*	Py4	13.2	This study	HQ-490	Py	15.6	Li et al. (2007b)
HZ-24	Gn	10.4	Meng (2014)	HQ-492	Py	16.0	Li et al. (2007b)
HZ-34	Gn	13.2	Meng (2014)	HQ-493	Py	15.8	Li et al. (2007b)
HZ-12	Py4	14.8	Meng (2014)	HQ-495	Py	16.2	Li et al. (2007b)
HZ-24	Py4	13.9	Meng (2014)	HQ-497	Py	16.7	Li et al. (2007b)
HZ-36	Py4	14.1	Meng (2014)	15.00	Sp	14.8	Li et al. (2007b)
HZ-40	Py4	13.2	Meng (2014)	8--1	Sp	15.5	Li et al. (2007b)
HZ-12	Sp	15.3	Meng (2014)	8--2	Sp	15.8	Li et al. (2007b)
HZ-15	Sp	14.0	Meng (2014)	H10–19-1	Sp	15.4	Li et al. (2007b)
HZ-17	Sp	12.5	Meng (2014)	H10–19-2	Sp	14.9	Li et al. (2007b)
HZ-22-1Q	Sp	13.3	Meng (2014)	H10–20-1	Sp	13.5	Li et al. (2007b)
HZ-22-1S	Sp	12.2	Meng (2014)	H10–20-2	Sp	14.2	Li et al. (2007b)
HZ-23	Sp	13.3	Meng (2014)	H10–20-3	Sp	14.5	Li et al. (2007b)
HZ-24	Sp	13.1	Meng (2014)	H10–20-4	Sp	14.2	Li et al. (2007b)
HZ-25	Sp	15.4	Meng (2014)	H10–22-1	Sp	13.6	Li et al. (2007b)
HZ-28	Sp	14.1	Meng (2014)	H10–3-1	Sp	15.3	Li et al. (2007b)
HZ-31	Sp	15.0	Meng (2014)	HQ-487	Sp	15.8	Li et al. (2007b)
HZ-32	Sp	15.0	Meng (2014)	HQ-488	Sp	16.0	Li et al. (2007b)
HZ-34	Sp	16.0	Meng (2014)	HQ-491	Sp	15.3	Li et al. (2007b)
HZ-35	Sp	15.7	Meng (2014)	HQ-493	Sp	13.5	Li et al. (2007b)
HZ-36	Sp	14.4	Meng (2014)	HQ-494	Sp	13.5	Li et al. (2007b)
HZ-38	Sp	13.5	Meng (2014)	HQ-495	Sp	13.4	Li et al. (2007b)
HZ-40	Sp	12.9	Meng (2014)	HQ-497	Sp	13.6	Li et al. (2007b)
HZ-41	Sp	15.3	Meng (2014)				

Table 2 (continued)

Sample no.	Mineral	$\delta^{34}S$ (‰)	References	Sample no.	Mineral	$\delta^{34}S$ (‰)	References
HZ-42	Sp	14.1	Meng (2014)				
HZ-43	Sp	15.0	Meng (2014)				

Samples in this study marked with asterisk represent sulfides were handpicked, other samples were collected by micro-drill. HZ-12 and MYMHZ-12 are from the same ore, HZ-24 and MYMHZ-24 are from the same ore, HZ-36 and MYMHZ-36 are from the same ore. *Py* pyrite, *Gn* galena, *Sp* sphalerite

trace elements in pyrite (e.g., Berner et al. 2013; Gregory et al. 2015) and characterize the trace element variations between different pyrite types, principal component analysis (PCA) was used based on an imputed dataset. The contents of elements below their detection limits are replaced by $DL/\sqrt{2}$ (Croghan and Egeghy 2003) because the statistical mean of censored data substituted with this value is close to the mean of the population (Verbovšek 2011). Data were then transformed using centered-log ratio (clr) method that is a suitable method for multivariate statistical techniques such as PCA (Egozcue et al. 2003; Huang et al. 2018). Three components (PC1-PC3) were extracted using eigenvalues over 1, which accounts for 60% of the variance in the dataset (Fig. 11). The biplots of loadings (e.g., PC1 vs. PC2) and scores (e.g., F1 vs. F2) are used to interpret the PCA results (Fig. 11).

As shown in Fig. 11a, elements in pyrite can be divided into three groups. Group 1 includes lattice-substituted elements As, Co, Ni, and Cu although Cu can also occur as inclusions, whereas Group 2 includes elements Ag, Sb, and Pb that commonly occur as inclusions (Huston et al. 1995). Group 1 can be further divided into two subgroups by the third principal component. Group 1a are elements As and Cu that occur as nonstoichiometric substitutions in the lattice, whereas Group 1b are elements Co and Ni that occur as stoichiometric

Fig. 10 Sulfur isotope histogram of sulfides from the Huize deposit. Pyrite has sulfur isotope values peaking between 14‰ and 18‰, whereas sphalerite has values peaking between 12‰ and 16‰. Galena has sulfur isotope values peaking between 10‰ and 12‰. *Py* pyrite, *Sp* sphalerite, *Gn* galena

substitutions for Fe (Huston et al. 1995) (Fig. 11c). Arsenic is the most abundant trace element in diagenetic pyrite and commonly substitutes for Fe in pyrite (Deditius et al. 2011). The positive correlation between As and Cu ($R^2 = 0.47$; Online Resource 3) is consistent with the high Cu contents found in As-bearing pyrite (Einaudi 1968; Griffin et al. 1991). The coupled behavior between As and Cu in pyrite is possibly due to coupled substitution of As and Cu with S because the substitution of As for S is commonly accompanied by the uptake of elements with ionic radii and charges similar to Fe^{2+} (e.g., Co^{2+}, Ni^{2+}, Cu^{2+}, Zn^{2+}) (Deditius et al. 2008). Group 3 consists of elements Te, Mn, Ti, Zn, Ge, Cr, and V. Tellurium may substitute S in pyrite, whereas Zn can occur as sphalerite inclusions (Huston et al. 1995). The occurrences of Mn, Ti, Ge, Cr, and V in pyrite are unclear. Germanium exhibits siderophile, lithophile, chalcophile, and organophile behaviors in different geologic environments (Bernstein 1985; Meng and Hu 2018). There is a weakly positive correlation between Ge and Zn ($R^2 = 0.34$; Online Resource 3), indicating that Ge may be hosted by sphalerite inclusions. This is consistent with the high Ge content in sphalerite from sphalerite–galena–pyrite assemblages (Höll et al. 2007; Belissont et al. 2014; Meng et al. 2015). However, the stronger positive correlation of Ge with Ti, V, Cr, and Mn ($R^2 = 0.73, 0.59, 0.49, 0.47$; Online Resource 3) indicates that Ge shows similar behavior with Ti, V, Cr, and Mn in pyrite. Elements such as Ti, V, and Cr are mainly hosted by a sedimentary matrix such as shale, whereas Mn can be hosted by both pyrite and sedimentary matrix (Thomas et al. 2011; Large et al. 2017). Considering that the main gangue minerals in the Huize deposit are carbonate minerals such as dolomite and calcite (Fig. 4), we conclude that Ti, V, Cr, Mn, and part of Ge, likely occur as carbonate inclusions in pyrite.

Variation in the spatial and temporal formation of pyrite allows inference to the trace element availability and variations in physicochemical conditions at the time of pyrite formation. Pyrite 1 has relatively high Cr, Ni, Zn, Ag, and Pb contents compared to other types (Fig. 8). As shown in Fig. 11d, Py1 is discriminated from other pyrite types by higher Pb, Co, and Ni contents. This indicates that ore-forming fluids were relatively rich in metals Co, Ni, Pb, Zn, and Ag in the early pyrite-sphalerite stage. Due to the absence of galena in this stage, elements Pb and Ag (a less extent for Zn) preferring partition into galena occur in pyrite as
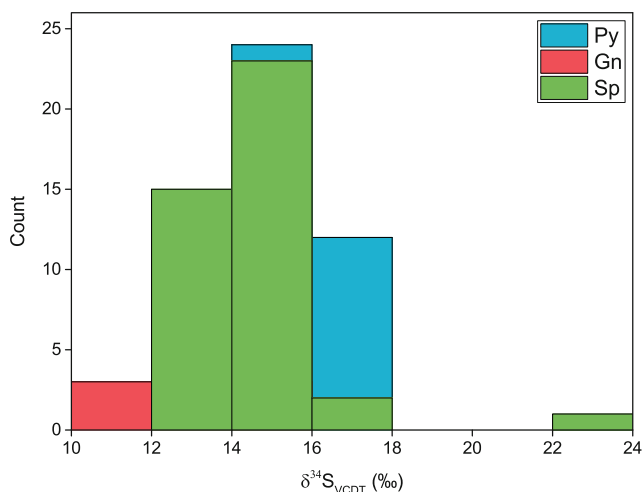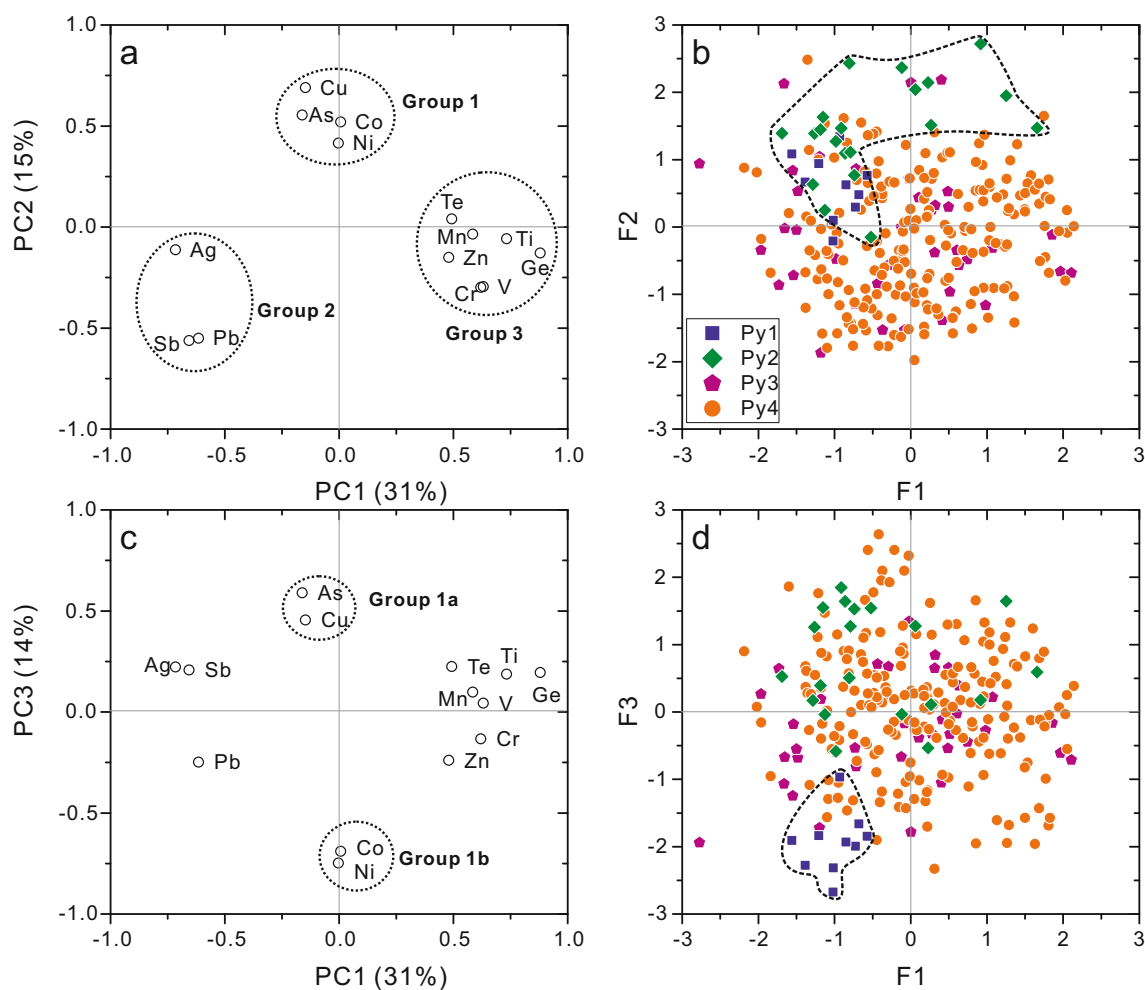
Fig. 11 Principle component analysis results of LA-ICP-MS trace element data of pyrite from the Huize deposit. **a** Plot of PC1 vs. PC2 (first and second loadings) showing correlations among trace elements in pyrite. **b** Plot of F1 vs. F2 (first and second scores) showing the distribution of different pyrite types in the latent variable space defined by PC1–PC2. **c** Plot of PC1 vs. PC3 (first and third loadings) showing correlations among trace elements in pyrite. **d** Plot of F1 vs. F3 (first and third scores) showing the distribution of different pyrite types in the latent variable space defined by PC1–PC3. The first, second, and third components account for 31%, 15%, and 14% of the variance in the dataset, respectively

inclusions. Pyrite 2 is discriminated from other pyrite types by higher Cu, As, Co, and Ni contents (Fig. 11c). But Py2 has lower Co and Ni contents than Py1 (Fig. 8) due to continued pyrite precipitation during fluid evolution, because these elements are lattice-substituted elements and mainly partitioned into pyrite in spite of co-existing sphalerite. The higher Cu and As contents in Py2 reflects the relative enrichment of these elements in fluids due to evolving fluids and absence of chalcopyrite in the pyrite-sphalerite stage. Pyrite 3 and Py4 have similar Mn, Co, Ni, Cu, As, Ag, Sb, and Pb contents (Fig. 8) and cannot be discriminated from each other by the defined PCA components (Fig. 11b and d), indicating similar fluids responsible for the formation of these two types of pyrite. Due to similar composition, Py3 and Py4 have overlapping fields in the plots Co versus Ni, As versus Cu, and Pb versus Ag and Sb (Fig. 9a-d). However, Py4 has slightly higher Ti, V, Cr, Ge, and Te contents than Py3 (Fig. 8) Higher Ti, V, and Cr in Py4

may reflect stronger carbonate replacement in the late sphalerite-galena-pyrite stage because these elements are mainly partitioned into carbonate inclusions in pyrite. This is evidenced by widespread replacement relic textures of Py4 that pyrite was replaced by carbonate minerals (Fig. 6c). In Pb-Zn ores, Ge prefers to enter into sphalerite than pyrite and galena (Meng et al. 2015), and thus slightly higher Ge contents in Py4 may be due to less co-precipitating sphalerite and more galena.

No obvious correlation of $\delta^{34}S$ with As, Pb, Zn, and Cu for Py3 and Py4 (Online Resource 4) indicates that factors controlling sulfur isotope fractionation (e.g., temperature, pH) didn't affect trace element partitioning into pyrite. The similar observation was reported in zoned pyrite from the El Indio Au-Cu-Ag deposit (Chile) where As, Cu, and Se do not co-vary with intracrystalline $\delta^{34}S$ (Tanner et al. 2016). This indicates that physicochemical conditions such as temperature,

pressure, and redox conditions have little influences on trace element variations in pyrite (e.g., George et al. 2016).

The source of sulfur

Sulfur is an important component for sulfide formation, and unraveling the source of sulfur is important to understand the origin of sulfide mineralization. Sphalerite, galena, and pyrite have high δ^{34}S values that range from 10.4 to 23.5‰ (Table 2 and Fig. 10), obviously different from that of magmatic sulfur (0‰; Taylor 1986). Gypsum and barite in the hosting Devonian to Permian strata have δ^{34}S values of ~15‰ and 28‰ (Liu and Lin 1999; Han et al. 2007), similar to those of Cambrian to Permian seawater sulfates (15‰ to 35‰; Claypool et al. 1980), indicative of a marine origin. The sulfur isotope composition of sulfides is comparable with that of gypsum and barite, and thus may have been derived from marine sulfates in the host rocks. A possible mechanism for producing reduced sulfur from sulfates includes bacterial sulfate reduction (BSR) and thermo-chemistry sulfate reduction (TSR). Bacterial sulfate reduction can produce sulfate–sulfide fractionations that typically range from 15‰ to 60‰ (Goldhaber and Kaplan 1982), whereas those associated with abiotic thermochemical reactions with organic compounds range from zero to as much as 10‰ (Orr 1974; Kiyosu 1980). Bacterial sulfate reduction commonly occurs at temperatures lower than about 110 °C (Jorgensen et al. 1992), whereas TSR is only effective at temperatures above about 125 °C because of slow reaction kinetics (Ohmoto 1992). The sulfur isotope composition of different sulfides shows a trend of $\delta^{34}S_{pyrite} > \delta^{34}S_{sphalerite} > \delta^{34}S_{galena}$, indicating that the sulfur of the ore-forming fluids has attained thermodynamic equilibrium (Ohmoto and Rye 1979). Mineralization temperature thus can be calculated using the sulfur isotope fractionation equation $\Delta^{34}S_{sphalerite-galena}$ (Ohmoto and Rye 1979). Sphalerite and galena mineral pairs from samples HZ-24 and HZ-34 are used for temperature calculation. The calculated equilibrium temperatures range from 170 to 300 °C, similar to the fluid inclusion homogenization temperatures of 150–240 °C for calcite and 100–344 °C for sphalerite (Han et al. 2007; Li 2010). Considering the relatively high formation temperatures (170–300 °C) and the positive δ^{34}S values of sulfides, we suggest that the sulfur of sulfides probably has derived from the thermochemical reduction of marine sulfates in the host strata.

The source of ore metals

The source of ore elements Pb and Zn can be inferred from the origin of pyrite assuming that metal elements Fe, Pb, and Zn have a common source. As discussed above, trace element composition of pyrite is controlled by the fluid composition and physicochemical conditions. Therefore, comparing the chemical composition of pyrite from different geological environments will help to identify the origin of pyrite and unravel the key factors inducing different types of mineralization (e.g., Meng et al. 2018). Pyrite from different types of deposits may have different trace element compositions. The Co/Ni ratio of pyrite is very useful in discriminating pyrite with different origins (Loftus-Hills and Solomon 1967; Bralia et al. 1979; Bajwah et al. 1987). Pyrite with high Co and Ni concentrations may be high-temperature, magmatic-hydrothermal in origin, and is related to mafic sources particularly where Co/Ni ratios are higher than unity in contrast to sedimentary environments where pyrite exhibits low Co/Ni ratios (Loftus-Hills and Solomon 1967; Bralia et al. 1979; Mookherjee and Philip 1979; Bajwah et al. 1987; Koglin et al. 2010; Large et al. 2014). Previous studies have shown that high Co/Ni ratios occur in pyrite from volcanogenic ores (~Co/Ni > 10), whereas lower temperature hydrothermal pyrite generally has Co/Ni ratios between ~5 and 10 (Bralia et al. 1979; Mookherjee and Philip 1979). A compilation of Co/Ni ratios by Bajwah et al. (1987) shows that pyrite from magmatic-hydrothermal deposits has Co/Ni ratios between ~1 and 10, whereas pyrite from orthomagmatic segregation deposits displays high but variable Co and Ni contents (up to wt% levels), and generally Co/Ni ratios of <1.

The Co/Ni ratios of pyrite from the Huize deposit are compared with those of pyrite from SEDEX and MVT deposits, sedimentary rocks, VMS deposits, submarine hydrothermal vents, and porphyry Cu, and iron oxide-copper-gold (IOCG) deposits (Fig. 12). Pyrite 1 shows limited variations of Co and Ni contents with Co/Ni ratios of ~0.01. All the analyses of Py1 plot in the field of SEDEX deposits (Fig. 12a). Pyrite 2, Py3, and Py4 from the Huize deposit have similar but variable Co and Ni contents and Co/Ni ratios ranging from 0.01 to 1. These three types of pyrite define a field separated from the field of SEDEX deposits (Fig. 12a). In general, pyrite from the Huize deposit has Co/Ni ratios lower than MVT deposits that have these ratios ranging from 0.2 to 7.2 (Fig. 12a). Minor analyses from Py2 and Py4 plot in the MVT field (Fig. 12a). All the analyses of Py1 and half of analyses of Py2, Py3, and Py4 plot in the field of sedimentary field (Fig. 12b). Nearly all the analyses of Py2, Py3, and Py4 plot in the field of submarine hydrothermal vents (Fig. 12d). All pyrite analyses from the Huize deposit define a field completely separated from VMS deposits, porphyry Cu deposits, and IOCG deposits (Fig. 12c–f), consistent with a non-magmatic (volcanic) hydrothermal origin. Some studies have concluded that Emeishan basalts have provided possible heat and ore metals for the Huize deposit by magmatic degassing (Huang et al. 2004). The lack of obvious magmatic-hydrothermal component in ore-forming fluids argues against the direct genetic link between the Emeishan basalts and Huize deposit. But Emeishan basalts may have provided some heat for the Huize deposit in terms of

Fig. 12 Plots of Co vs. Ni contents in pyrite from Huize deposit. Microanalytical data for pyrite from other deposit/rock types are shown as gray fields except pyrite from MVT Zn-Pb deposits as a dotted polygon. **a** SEDEX (Howard's Pass district of Canada, McArthur Basin of Australia) (Gadd et al. 2016; Mukherjee and Large 2017) and MVT deposits (Jinding and Hoshbulak, China) (Li et al. 2015; Wang et al. 2018). **b** Sedimentary pyrite (Worldwide) (Berner et al. 2013; Large et al. 2014; Gregory et al. 2017; Mukherjee and Large 2017). **c** VMS deposits (Keketale in Altay of NW China, Bathurst and Matagami districts of Canada, Pontide of NE Turkey) (Zheng et al. 2013; Revan et al. 2014; Genna and Gaboury 2015; Soltani Dehnavi et al. 2015). **d** Submarine hydrothermal vents (Keith et al. 2016). **e** Porphyry Cu deposits (Dexing and Jinchang of China, Metaliferi Mountains of Romania) (Reich et al. 2013; Cioacă et al. 2014; Zhang et al. 2016). **f** IOCG deposits (Ernest Henry of Australia and Manto Verde of Chile) (Rieger et al. 2010; Rusk et al. 2010)
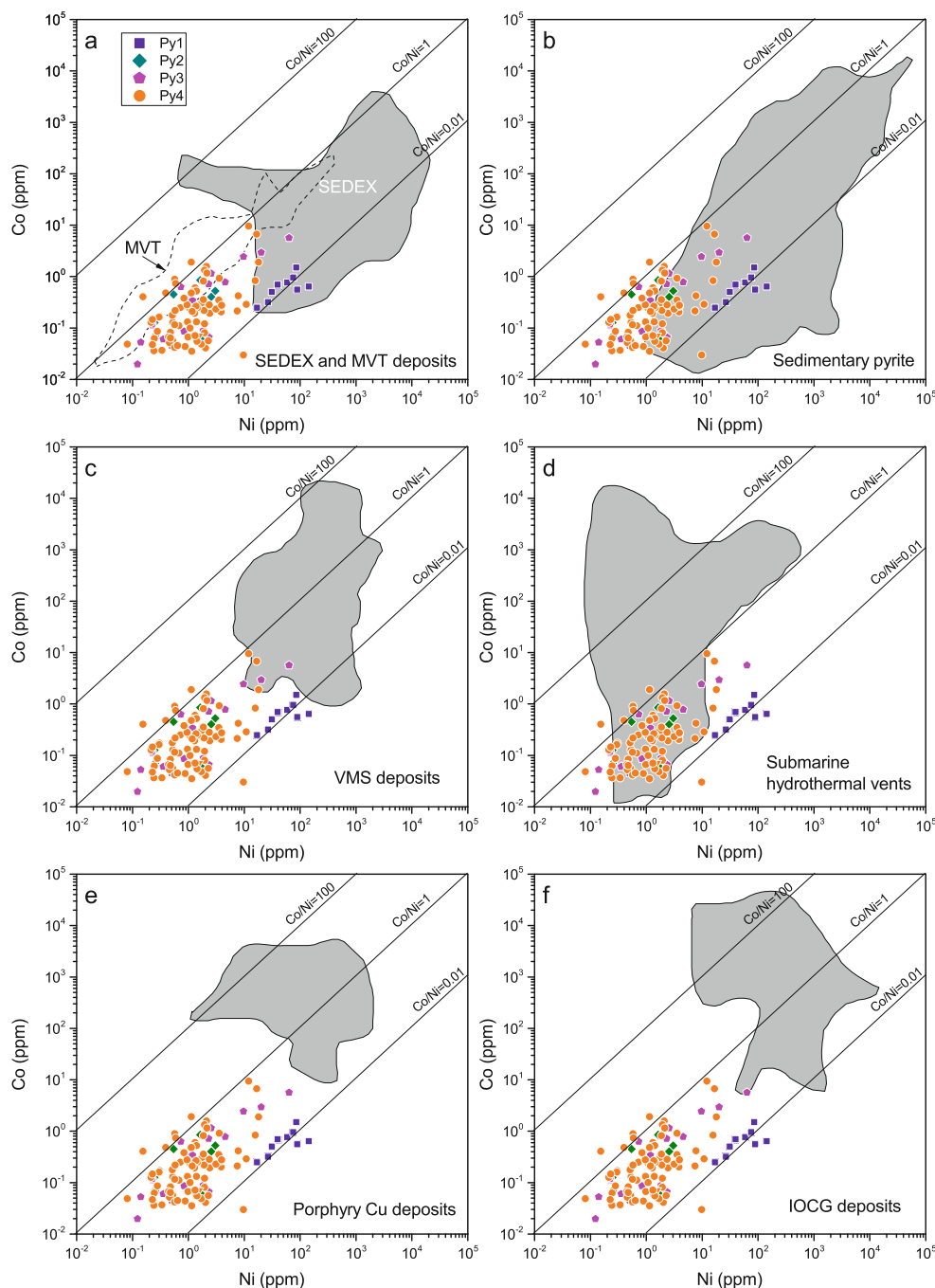
higher formation temperature (170–300 °C) than typical MVT deposits (<150 °C) (Leach et al. 2001).

Comparison with MVT Zn-Pb deposits

Mississippi Valley-type Zn-Pb deposits are hosted in basin-margin carbonate platform sedimentary rocks and commonly consist of coarse galena and sphalerite that fill open spaces in brecciated and dolomitized limestones (Anderson and Macqueen 1982; Leach et al. 2001). Ore fluids are relatively

low temperature (<150 °C), highly saline, sulfate-bearing basinal brines that precipitate galena and sphalerite by reduction of sulfate to metal sulfide (Anderson 1991; Leach et al. 2001; Kesler and Reich 2006). Han et al. (2007) showed that the Huize deposit has a lot of features similar to typical MVT Zn-Pb deposits in terms of tectonic setting, deposit geology, wall-rock alteration, and mineral trace element and isotope composition. They emphasized the regionally tectonic or locally structural controlling on the formation of the Huize deposit and designated this deposit as a deformed, carbonate-

hosted, MVT deposit. However, the Huize deposit displays some unique geological and geochemical features that distinguish it from typical MVT Zn-Pb deposits. These include the distinct ore features, homogenization temperatures of fluid inclusions, pyrite trace element composition, and relationship to magmatic rocks.

The high-grade Pb-Zn ores are rich in metals Ag, Ge, In, Ga, Cd, and Tl (Han et al. 2007). Moreover, Ag and Ge are mined as economic elements because Ag grades at 46–100 g/t and Ge grades at 30–81 g/t (Huang et al. 2004). This makes the Huize deposit as an important Ge-rich deposit that is comparable to Wulantuga Ge deposit of Inner Mongolia in China (Meng 2014). Fluid inclusions of sphalerite and calcite have homogenization temperatures ranging from 100 to 344 °C (Han et al. 2007; Li 2010). The Ag grade and fluid inclusion homogenization temperatures of the Huize Zn-Pb ores are different from typical MVT ores that contain <~10 g/t Ag and form at <150 °C (Titley 1996; Bonsall et al. 2011; Online Resource 4). The Huize ores have Ag contents and homogenization temperatures comparable to Irish Pb-Zn ores and high-temperature carbonate-replacement Pb-Zn ores (Online Resource 4), indicating that hydrothermal replacement may play an important role in the formation of the Huize deposit.

Pyrite from the Huize deposit has the chemical composition (Co, Ni concentrations and Co/Ni ratios) similar to pyrite formed in marine environments, i.e., SEDEX deposits, sedimentary pyrite, and submarine hydrothermal vents. This may reflect the similar basinal brine or seawater origin for these deposits (Cooke et al. 2000; Large et al. 2017). Sulfur isotope data also indicate that sulfur of sulfides probably has derived from the thermochemical reduction of marine sulfates in the host strata. However, pyrite from the Huize deposit has Co/Ni ratios lower than that from MVT Zn-Pb deposits such as Jinding and Hoshbulak (Fig. 12a). Pyrite from the Huize deposit has Co and Ni contents obviously lower than that from VMS, porphyry Cu, and IOCG deposits that formed at relatively high temperature (~250–500 °C) (Ohmoto 1996; Large et al. 2001; Schardt et al. 2001; Franklin et al. 2005; Williams et al. 2005; Sillitoe 2010). Porphyry Cu and IOCG deposits are mainly derived from magmatic-hydrothermal fluids, whereas VMS deposits are derived from circulated seawater or basinal brines with possible involvement of magmatic component. Therefore, the Huize deposit is different from typical MVT Zn-Pb deposits and magmatic-hydrothermal deposits. Therefore, the Huize deposit was most likely derived from low to moderate temperature, basin brine-derived ore-forming fluids without the significant contribution of a magmatic component. The Huize deposit can be thus defined as a transitional type between MVT and high-temperature carbonate-replacement Zn-Pb deposits.

Conclusions

Pyrite with zoned texture was formed by multiple ore fluids or dissolution and reprecipitation processes, whereas pyrite with replacement relic texture was formed by replacement of pyrite by late Pb-Zn-rich fluids. Trace element variation in Huize pyrite results from a combination of mineral inclusions, co-precipitating minerals, and variations in fluid compositions. The sulfur of sulfides probably has derived from the thermochemical reduction of marine sulfates. The low to intermediate formation temperature and basin brine-derived ore-forming fluids without a contribution of magmatic components may explain the trace element characteristic of pyrite from the Huize deposit. We conclude that no direct genetic link between Permian Emeishan basalts and Pb-Zn mineralization in the Huize deposit. But the involvement of magmatic heat cannot be precluded. We consider that the Huize deposit is a transitional type between MVT and high-temperature carbonate-replacement Zn-Pb deposits.

References

Abraitis PK, Pattrick RAD, Vaughan DJ (2004) Variations in the compositional, textural and electrical properties of natural pyrite: a review. Int J Miner Process 74:41–59

Anderson GM (1991) Organic maturation and ore precipitation in Southeast Missouri. Econ Geol 86:909–926

Anderson GM, Macqueen RW (1982) Ore deposit models-6. Mississippi Valley-type lead-zinc deposits. Geosci Can 9:108–117

Bajwah ZU, Seccombe PK, Offler R (1987) Trace element distribution, Co: Ni ratios and genesis of the Big Cadia iron-copper deposit, New South Wales, Australia. Miner Deposita 22:292–300

Baker T, Mustard R, Brown V, Pearson N, Stanley C, Radford N, Butler I (2006) Textural and chemical zonation of pyrite at Pajingo: a potential vector to epithermal gold veins. Geochem Explor Environ Anal 6:283–293

Belissont R, Boiron M-C, Luais B, Cathelineau M (2014) LA-ICP-MS analyses of minor and trace elements and bulk Ge isotopes in zoned Ge-rich sphalerites from the Noailhac–Saint-Salvy deposit (France): Insights into incorporation mechanisms and ore deposition processes. Geochim Cosmochim Acta 126:518–540

Berner ZA, Puchelt H, Noeltner T, Kramar UTZ (2013) Pyrite geochemistry in the Toarcian Posidonia Shale of south-west Germany:

Evidence for contrasting trace-element patterns of diagenetic and syngenetic pyrites. Sedimentology 60:548–573

Bernstein LR (1985) Germanium geochemistry and mineralogy. Geochim Cosmochim Acta 49:2409–2422

Bonsall TA, Spry PG, Voudouris PC, Tombros S, Seymour KS, Melfos V (2011) The geochemistry of carbonate-replacement Pb-Zn-Ag mineralization in the Lavrion district, Attica, Greece: Fluid inclusion, stable isotope, and rare earth element studies. Econ Geol 106:619–651

Bralia A, Sabatini G, Troja F (1979) A revaluation of the Co/Ni ratio in pyrite as geochemical tool in ore genesis problems. Miner Deposita 14:353–374

Chung S-L, B-m J (1995) Plume-lithosphere interaction in generation of the Emeishan flood basalts at the Permian-Triassic boundary. Geology 23:889–892

Cioacă ME, Munteanu M, Qi L, Costin G (2014) Trace element concentrations in porphyry copper deposits from Metaliferi Mountains, Romania: A reconnaissance study. Ore Geol Rev 63:22–39

Claypool GE, Holser WT, Kaplan IR, Sakai H, Zak I (1980) The age curves of sulfur and oxygen isotopes in marine sulfate and their mutual interpretation. Chem Geol 28:199–260

Cook N, Ciobanu CL, George L, Zhu Z-Y, Wade B, Ehrig K (2016) Trace element analysis of minerals in magmatic-hydrothermal ores by laser ablation inductively-coupled plasma mass spectrometry: Approaches and opportunities. Minerals 6:1–34

Cook NJ, Ciobanu CL, Mao J (2009) Textural control on gold distribution in As-free pyrite from the Dongping, Huangtuliang and Hougou gold deposits, North China Craton (Hebei Province, China). Chem Geol 264:101–121

Cooke DR, Bull SW, Large RR, McGoldrick PJ (2000) The importance of oxidized brines for the formation of Australian Proterozoic stratiform sediment-hosted Pb-Zn (Sedex) deposits. Econ Geol 95:1–18

Croghan CW, Egeghy PP (2003) Methods of dealing with values below the limit of detection using SAS. Southeastern SAS User Group (City, 22–24 September 2003)

Deditius AP, Reich M, Kesler SE, Utsunomiya S, Chryssoulis SL, Walshe J, Ewing RC (2014) The coupled geochemistry of Au and As in pyrite from hydrothermal ore deposits. Geochim Cosmochim Acta 140:644–670

Deditius AP, Utsunomiya S, Reich M, Kesler SE, Ewing RC, Hough R, Walshe J (2011) Trace metal nanoparticles in pyrite. Ore Geol Rev 42:32–46

Deditius AP, Utsunomiya S, Renock D, Ewing RC, Ramana CV, Becker U, Kesler SE (2008) A proposed new type of arsenian pyrite: Composition, nanostructure and geological significance. Geochim Cosmochim Acta 72:2919–2933

Deol S, Deb M, Large RR, Gilbert S (2012) LA-ICPMS and EPMA studies of pyrite, arsenopyrite and loellingite from the Bhukia-Jagpura gold prospect, southern Rajasthan, India: Implications for ore genesis and gold remobilization. Chem Geol 326-327:72–87

Egozcue JJ, Pawlowsky-Glahn V, Mateu-Figueras G, Barcelo-Vidal C (2003) Isometric logratio transformations for compositional data analysis. Math Geol 35:279–300

Einaudi MT (1968) Copper zoning in pyrite from Cerro de Pasco, Peru. Am Mineral 53:1748–1752

Franchini M, McFarlane C, Maydagán L, Reich M, Lentz DR, Meinert L, Bouhier V (2015) Trace metals in pyrite and marcasite from the Agua Rica porphyry-high sulfidation epithermal deposit, Catamarca, Argentina: Textural features and metal zoning at the porphyry to epithermal transition. Ore Geol Rev 66:366–387

Franklin JM, Gibson HL, Jonasson IR, Galley AG (2005) Volcanogenic massive sulfide deposits. Econ Geol 100th Ann Vol: 523–560

Fu S, Gu X, Wang Q, Liu X (2003) Lead isotopic geochemistry and its bearing on genesis of the Huize Pb-Zn deposit, Yunnan, South China. Geochim Cosmochim Acta 67:A107

Gadd MG, Layton-Matthews D, Peter JM, Paradis SJ (2016) The world-class Howard's Pass SEDEX Zn-Pb district, Selwyn Basin, Yukon.

Part I: trace element compositions of pyrite record input of hydrothermal, diagenetic, and metamorphic fluids to mineralization. Miner Deposita 51:319–342

Gao J-F, Jackson SE, Dubé B, Kontak DJ, De Souza S (2015) Genesis of the Canadian Malartic, Côté Gold, and Musselwhite gold deposits: Insights from LA-ICP-MS element mapping of pyrite. In: Dubé B, Mercier-Langevin P (eds) Targeted Geoscience Initiative 4: Contributions to the Understanding of Precambrian Lode Gold Deposits and Implications for Exploration. Geol Surv Can Open File 7852, pp 157–175

Gao S, Yang J, Zhou L, Li M, Hu Z, Guo J, Yuan H, Gong H, Xiao G, Wei J (2011) Age and growth of the Archean Kongling terrain, South China, with emphasis on 3.3 Ga granitoid gneisses. Am J Sci 311: 153–182

Genna D, Gaboury D (2015) Deciphering the hydrothermal evolution of a VMS system by LA-ICP-MS using trace elements in pyrite: An example from the Bracemac-McLeod deposits, Abitibi, Canada, and implications for exploration. Econ Geol 110:2087–2108

George LL, Cook NJ, Ciobanu CL (2016) Partitioning of trace elements in co-crystallized sphalerite–galena–chalcopyrite hydrothermal ores. Ore Geol Rev 77:97–116

Goldhaber MB, Kaplan IR (1982) Controls and consequences of sulfate reduction rates in recent marine sediments. Acid Sulfate Weathering 119:19–36

Gregory DD, Large RR, Bath AB, Steadman JA, Wu S, Danyushevsky L, Bull SW, Holden P, Ireland TR (2016) Trace Element Content of Pyrite from the Kapai Slate, St. Ives Gold District, Western Australia. Econ Geol 111:1297–1320

Gregory DD, Large RR, Halpin JA, Baturina EL, Lyons TW, Wu S, Danyushevsky L, Sack PJ, Chappaz A, Maslennikov VV (2015) Trace element content of sedimentary pyrite in black shales. Econ Geol 110:1389–1410

Gregory DD, Lyons TW, Large RR, Jiang G, Stepanov AS, Diamond CW, Figueroa MC, Olin P (2017) Whole rock and discrete pyrite geochemistry as complementary tracers of ancient ocean chemistry: An example from the Neoproterozoic Doushantuo Formation, China. Geochim Cosmochim Acta 216:201–220

Griffin WL, Ashley PM, Ryan CG, Sie SH, Suter GF (1991) Pyrite geochemistry in the North Arm epithermal Ag-Au deposit, Queensland, Australia; a proton-microprobe study. Can Miner 29: 185–198

Höll R, Kling M, Schroll E (2007) Metallogenesis of germanium—A review. Ore Geol Rev 30:145–180

Halicz L, Günther D (2004) Quantitative analysis of silicates using LA-ICP-MS with liquid calibration. J Anal At Spectrom 19:1539–1545

Han RS, Liu CQ, Huang ZL, Ma DY, Li Y, Hu B, Ma GS, Lei L (2004) Fluid inclusions of calcite and sources of ore-forming fluids in the Huize Zn-Pb-(Ag-Ge) district, Yunnan, China. Acta Geol Sin 78: 583–591

Han RS, Liu CQ, Huang ZL, Chen J, Ma DY, Lei L, Ma GS (2007) Geological features and origin of the Huize carbonate-hosted Zn-Pb-(Ag) district, Yunnan, South China. Ore Geol Rev 31:360–383

Hu R-Z, Zhou M-F (2012) Multiple Mesozoic mineralization events in South China—an introduction to the thematic issue. Miner Deposita 47:579–588

Hu RZ, Fu SL, Huang Y, Zhou MF, Fu SH, Zhao CH, Wang YJ, Bi XW, Xiao JF (2017) The giant South China Mesozoic low-temperature metallogenic domain: Reviews and a new geodynamic model. J Asian Earth Sci 137:9–34

Huang X-W, Boutroy É, Makvandi S, Beaudoin G, Corriveau L, De Toni AF (2018) Trace element composition of iron oxides from IOCG and IOA deposits: relationship to hydrothermal alteration and deposit subtypes. Miner Deposita. https://doi.org/10.1007/s00126-018-0825-1

Huang Z, Li W, Chen J, Xu D, Han R, Liu C (2001) Carbon and oxygen isotope geochemistry of the Huize superlarge Pb-Zn Ore deposits in Yunnan Province. Geotecton Metallogen 28:53–59 (in Chinese with English abstract)

Huang ZL, Chen J, Han RS, Li WB, Liu CQ, Zhang ZL, Ma DY, Gao DR, Yang HL (2004) Geochemistry and ore-formation of the Huize giant lead-zinc deposit, Yunnan, Province, China: Discussion on the relationship between Emeishan flood basalts and lead-zinc mineralization. Geological Publishing House, Beijing (in Chinese)

Huang ZL, Li WB, Chen J, Han RS, Liu CQ, Xu C, Guan T (2003) Carbon and oxygen isotope constraints on mantle fluid involvement in the mineralization of the Huize super-large Pb-Zn deposits, Yunnan Province, China. J Geochem Explor 78:637–642

Huston DL, Sie SH, Suter GF, Cooke DR, Both RA (1995) Trace elements in sulfide minerals from eastern Australian volcanic-hosted massive sulfide deposits; Part I, Proton microprobe analyses of pyrite, chalcopyrite, and sphalerite, and Part II, Selenium levels in pyrite; comparison with delta ^{34}S values and implications for the source of sulfur in volcanogenic hydrothermal systems. Econ Geol 90:1167–1196

Jorgensen BB, Isaksen MF, Jannasch HW (1992) Bacterial sulfate reduction above 100 degrees Celsius in deep-sea hydrothermal vent sediments. Science 258:1756–1758

Keith M, Häckel F, Haase KM, Schwarz-Schampera U, Klemd R (2016) Trace element systematics of pyrite from submarine hydrothermal vents. Ore Geol Rev 72:728–745

Kesler SE, Reich MH (2006) Precambrian Mississippi Valley-type deposits: relation to changes in composition of the hydrosphere and atmosphere. Geol Soc Am Memoir 198:185–204

Kiyosu Y (1980) Chemical reduction and sulfur-isotope effects of sulfate by organic matter under hydrothermal conditions. Chem Geol 30:47–56

Koglin N, Frimmel HE, Minter WL, Brätz H (2010) Trace-element characteristics of different pyrite types in Mesoarchaean to Palaeoproterozoic placer deposits. Miner Deposita 45:259–280

Large RR, Danyushevsky L, Hollit C, Maslennikov V, Meffre S, Gilbert S, Bull S, Scott R, Emsbo P, Thomas H (2009) Gold and trace element zonation in pyrite using a laser imaging technique: implications for the timing of gold in orogenic and Carlin-style sediment-hosted deposits. Econ Geol 104:635–668

Large RR, Gemmell JB, Paulick H, Huston DL (2001) The alteration box plot: A simple approach to understanding the relationship between alteration mineralogy and lithogeochemistry associated with volcanic-hosted massive sulfide deposits. Econ Geol 96:957–971

Large RR, Halpin JA, Danyushevsky LV, Maslennikov VV, Bull SW, Long JA, Gregory DD, Lounejeva E, Lyons TW, Sack PJ (2014) Trace element content of sedimentary pyrite as a new proxy for deep-time ocean–atmosphere evolution. Earth Planet Sci Lett 389:209–220

Large RR, Mukherjee I, Gregory DD, Steadman JA, Maslennikov VV, Meffre S (2017) Ocean and atmosphere geochemical proxies derived from trace elements in marine pyrite: Implications for ore genesis in sedimentary basins. Econ Geol 112:423–450

Leach DL, Bradley D, Lewchuk MT, Symons DT, de Marsily G, Brannon J (2001) Mississippi Valley-type lead–zinc deposits through geological time: implications from recent age-dating research. Miner Deposita 36:711–740

Leach DL, Bradley DC, Huston D, Pisarevsky SA, Taylor RD, Gardoll SJ (2010) Sediment-hosted lead-zinc deposits in Earth history. Econ Geol 105:593–625

Li B (2010) The Study of Fluid Inclusions Geochemistry and Tectonic Geochemistry of Lead-Zinc Deposits: Taking Huize and Songliang Lead-Zinc Deposits for Examples, in the Northeast of Yunnan Province, China. PhD thesis, Kunming University of Science and Technology, Kunming (in Chinese with English abstract)

Li W, Huang Z, Yin M (2007a) Dating of the Giant Huize Zn-Pb Ore Field of Yunnan Province, Southwest China: Constraints from the Sm-Nd System in Hydrothermal Calcite. Resour Geol 57:90–97

Li W, Huang Z, Yin M (2007b) Isotope geochemistry of the Huize Zn-Pb ore field, Yunnan Province, Southwestern China: Implication for the sources of ore fluid and metals. Geochem J 41:65–81

Li WB, Huang ZL, Qi L (2007c) REE geochemistry of sulfides from the Huize Zn-Pb ore field, Yunnan Province: implication for the sources of ore-forming metals. Acta Geol Sin 81:442–449

Li XB, Huang ZL, Li W, Zhang ZL, Yan ZF (2006) Sulfur isotopic compositions of the Huize super-large Pb–Zn deposit, Yunnan Province, China: implications for the source of sulfur in the ore-forming fluids. J Geochem Explor 89:227–230

Li Z, Xue C, Wu Y, Dong X, Wang S, Chen J (2015) The nappe-hosted Hoshbulak MVT Zn–Pb deposit, Xinjiang, China: A review of the geological, elemental and stable isotopic constraints. Ore Geol Rev 70:47–60

Liu HC, Lin WD (1999) Study on the law of Pb-Zn-Ag ore deposit in Northeast Yunnan, China. Yunnan University Press, Kunming, pp 1–468 (in Chinese)

Loftus-Hills G, Solomon M (1967) Cobalt, nickel and selenium in sulphides as indicators of ore genesis. Miner Deposita 2:228–242

Meng YM (2014) Application of Ge isotopes to mineral deposits: Examples from the Wulantuga Ge deposit of Inner Mongolia, the Huize and other Pb-Zn deposits of SW China. PhD thesis, University of Chinese Academy of Sciences, Beijing, pp 1–142 (in Chinese with English abstract)

Meng Y-M, Hu R-Z (2018) Minireview: Advances in Germanium Isotope Analysis by Multiple Collector-Inductively Coupled Plasma-Mass Spectrometry. Anal Lett 51:627–647

Meng Y-M, Hu R-Z, Huang X-W, Gao J-F, Qi L, Lyu C (2018) The relationship between volcanic-associated massive sulfide mineralization and porphyry-skarn Mo mineralization in the Laochang deposit, SW China: Constraints from Re-Os isotopes, sulfur isotopes and in situ trace elements of pyrite. J Geochem Explor 194:218–238

Meng Y-M, Qi H-W, Hu R-Z (2015) Determination of germanium isotopic compositions of sulfides by hydride generation MC-ICP-MS and its application to the Pb–Zn deposits in SW China. Ore Geol Rev 65:1095–1109

Mookherjee A, Philip R (1979) Distribution of copper, cobalt and nickel in ores and host-rocks, Ingladhal, Karnataka, India. Miner Deposita 14:33–55

Mukherjee I, Large R (2017) Application of pyrite trace element chemistry to exploration for SEDEX style Zn-Pb deposits: McArthur Basin, Northern Territory, Australia. Ore Geol Rev 81:1249–1270

Ohmoto H (1992) Biogeochemistry of sulfur and the mechanisms of sulfide-sulfate mineralization in Archean oceans. In: Schidlowski M, Golubic S, Kimberley MM, Mckirdy DM, Trudinger PA (eds) Early Organic Evolution: Implications for Mineral and Energy Resources. Springer-Verlag, pp 378–397

Ohmoto H (1996) Formation of volcanogenic massive sulfide deposits: the Kuroko perspective. Ore Geol Rev 10:135–177

Ohmoto H, Rye RO (1979) Isotopes of sulfur and carbon. Geochemistry of hydrothermal ore deposits. Wiley, New York

Orr WL (1974) Changes in sulfur content and isotopic ratios of sulfur during petroleum maturation; study of big horn basin paleozoic oils. AAPG Bull 58:2295–2318

Pačevski A, Moritz R, Kouzmanov K, Marquardt K, Živković P, Cvetković L (2012) Texture and composition of Pb-bearing pyrite from the Čoka Marin polymetallic deposit, Serbia, controlled by nanoscale inclusions. Can Miner 50:1–20

Qiu YM, Gao S, McNaughton NJ, Groves DI, Ling W (2000) First evidence of >3.2 Ga continental crust in the Yangtze craton of south

China and its implications for Archean crustal evolution and Phanerozoic tectonics. Geology 28:11–14

Reich M, Deditius A, Chryssoulis S, Li J-W, Ma C-Q, Parada MA, Barra F, Mittermayr F (2013) Pyrite as a record of hydrothermal fluid evolution in a porphyry copper system: A SIMS/EMPA trace element study. Geochim Cosmochim Acta 104:42–62

Reich M, Kesler SE, Utsunomiya S, Palenik CS, Chryssoulis SL, Ewing RC (2005) Solubility of gold in arsenian pyrite. Geochim Cosmochim Acta 69:2781–2796

Reich M, Simon AC, Deditius A, Barra F, Chryssoulis S, Lagas G, Tardani D, Knipping J, Bilenker L, Sánchez-Alfaro P (2016) Trace element signature of pyrite from the Los Colorados iron oxide-apatite (IOA) deposit, Chile: a missing link between Andean IOA and iron oxide copper-gold systems? Econ Geol 111:743–761

Reid A, Wilson CJ, Shun L, Pearson N, Belousova E (2007) Mesozoic plutons of the Yidun Arc, SW China: U/Pb geochronology and Hf isotopic signature. Ore Geol Rev 31:88–106

Revan MK, Genç Y, Maslennikov VV, Maslennikova SP, Large RR, Danyushevsky LV (2014) Mineralogy and trace-element geochemistry of sulfide minerals in hydrothermal chimneys from the Upper-Cretaceous VMS deposits of the eastern Pontide orogenic belt (NE Turkey). Ore Geol Rev 63:129–149

Rieger AA, Marschik R, Díaz M, Hölzl S, Chiaradia M, Akker B, Spangenberg JE (2010) The hypogene iron oxide copper-gold mineralization in the Mantoverde district, Northern Chile. Econ Geol 105:1271–1299

Rusk B, Oliver N, Cleverley J, Blenkinsop T, Zhang D, Williams P, Habermann P (2010) Physical and chemical characteristics of the Ernest Henry iron oxide copper gold deposit, Australia; implications for IOCG genesis. In: Porter TM (ed) Hydrothermal Iron Oxide Copper-Gold & Related Deposits: A Global Perspective, vol 3. PGC Publishing, Adelaide, pp 1–18

Schardt C, Cooke DR, Gemmell JB, Large RR (2001) Geochemical modeling of the zoned footwall alteration pipe, Hellyer volcanic-hosted massive sulfide deposit, Western Tasmania, Australia. Econ Geol 96:1037–1054

Sillitoe RH (2010) Porphyry copper systems. Econ Geol 105:3–41

Soltani Dehnavi A, Lentz DR, McFarlane CRM (2015) LA-ICP-MS analysis of volatile trace elements in massive sulphides and host rocks of selected VMS deposits of the Bathurst mining camp, New Brunswick: Methodology and application to exploration. In: Peter JM, Mercier-Langevin P (eds) Targeted Geoscience Initiative 4: Contributions to the Understanding of Volcanogenic Massive Sulphide Deposit Genesis and Exploration Methods Development. Geol Surv Can Open File 7853, pp 59–80

Sun WH, Zhou MF, Gao JF, Yang YH, Zhao XF, Zhao JH (2009) Detrital zircon U-Pb geochronological and Lu-Hf isotopic constraints on the Precambrian magmatic and crustal evolution of the western Yangtze Block, SW China. Precambrian Res 172:99–126

Tanner D, Henley RW, Mavrogenes JA, Holden P (2016) Sulfur isotope and trace element systematics of zoned pyrite crystals from the El Indio Au–Cu–Ag deposit, Chile. Contrib Mineral Petrol 171:1–17

Taylor BE (1986) Magmatic volatiles: isotope variation of C, H and S. In: Reviews in mineralogy, vol 16. Stable isotopes on high temperature geological process. Miner Soc Amer, pp 185–226

Thomas HV, Large RR, Bull SW, Maslennikov V, Berry RF, Fraser R, Froud S, Moye R (2011) Pyrite and pyrrhotite textures and composition in sediments, laminated quartz veins, and reefs at Bendigo gold mine, Australia: insights for ore genesis. Econ Geol 106:1–31

Titley SR (1996) Characteristics of high temperature, carbonate-hosted replacement ores and some comparisons with Mississippi Valley-type ores. Soc Econ Geol Spec Publ 4:244–254

Verbovšek T (2011) A comparison of parameters below the limit of detection in geochemical analyses by substitution methods. Mater Geoenviron 58:393–404

Wang C, Yang L, Bagas L, Evans NJ, Chen J, Du B (2018) Mineralization processes at the giant Jinding Zn–Pb deposit, Lanping Basin, Sanjiang Tethys Orogen: Evidence from in situ trace element analysis of pyrite and marcasite. Geol J 53:1279–1294

Williams PJ, Barton MD, Johnson DA, Fontbote L, De Haller A, Mark G, Oliver NHS, Marschik R (2005) Iron oxide copper-gold deposits: geology, space-time distribution and possible modes of origin. Econ Geol 100th Ann Vol: 371–405

Wohlgemuth-Ueberwasser CC, Viljoen F, Petersen S, Vorster C (2015) Distribution and solubility limits of trace elements in hydrothermal black smoker sulfides: An in-situ LA-ICP-MS study. Geochim Cosmochim Acta 159:16–41

Yan D-P, Zhou M-F, Song H-L, Wang X-W, Malpas J (2003) Origin and tectonic significance of a Mesozoic multi-layer over-thrust system within the Yangtze Block (South China). Tectonophysics 361:239–254

Ye L, Cook NJ, Ciobanu CL, Liu Y, Zhang Q, Liu T, Gao W, Yang Y, Danyushevskiy L (2011) Trace and minor elements in sphalerite from base metal deposits in South China: A LA-ICPMS study. Ore Geol Rev 39:188–217

Zhang CQ, Mao JW, Liu F, Li HM (2005a) K-Ar dating of altered clay minerals from Huize Pb-Zn deposit in Yunnan Province and its geological significance. Mineral Deps 24:317–324 (in Chinese with English abstract)

Zhang P, Huang X-W, Cui B, Wang B-C, Yin Y-F, Wang J-R (2016) Re-Os isotopic and trace element compositions of pyrite and origin of the Cretaceous Jinchang porphyry Cu-Au deposit, Heilongjiang Province, NE China. J Asian Earth Sci 129:67–80

Zhang Z, Huang Z, Guan T, Yan Z, Gao D (2005b) Study on the multi-sources of ore-forming materials and ore-forming fluids in the Huize lead-zinc ore deposit. Chin J Geochem 24:243–252

Zhao JH, Zhou MF, Yan DP, Zheng JP, Li JW (2011) Reappraisal of the ages of Neoproterozoic strata in South China: No connection with the Grenvillian orogeny. Geology 39:299–302

Zheng Y, Zhang L, Y-j C, Hollings P, H-y C (2013) Metamorphosed Pb–Zn–(Ag) ores of the Keketale VMS deposit, NW China: evidence from ore textures, fluid inclusions, geochronology and pyrite compositions. Ore Geol Rev 54:167–180

Zhou C, Wei C, Guo J, Li C (2001) The source of metals in the Qilinchang Zn-Pb deposit, Northeastern Yunnan, China: Pb-Sr isotope constraints. Econ Geol 96:583–598

Zhou JC, Wang XL, Qiu JS (2009) Geochronology of Neoproterozoic mafic rocks and sandstones from northeastern Guizhou, South China: Coeval arc magmatism and sedimentation. Precambrian Res 170:27–42

Zhou M-F, Arndt NT, Malpas J, Wang CY, Kennedy AK (2008) Two magma series and associated ore deposit types in the Permian Emeishan large igneous province, SW China. Lithos 103:352–368

Zhou MF, Yan DP, Kennedy AK, Li Y, Ding J (2002) SHRIMP U-Pb zircon geochronological and geochemical evidence for Neoproterozoic arc-magmatism along the western margin of the Yangtze Block, South China. Earth Planet Sci Lett 196:51–67

Zwahlen C, Cioldi S, Wagner T, Rey R, Heinrich C (2014) The porphyry Cu-(Mo-Au) deposit at Altar (Argentina): Tracing gold distribution by vein mapping and LA-ICP-MS mineral analysis. Econ Geol 109:1341–1358

Affiliations

Yu-Miao Meng[1] · Rui-Zhong Hu[1,2] · Xiao-Wen Huang[1] · Jian-Feng Gao[1] · Christian Sasseville[3,4]

[1] State Key Laboratory of Ore Deposit Geochemistry, Institute of Geochemistry, Chinese Academy of Sciences, Guiyang 550081, China

[2] College of Earth and Planetary Sciences, University of Chinese Academy of Sciences, Beijing 100049, China

[3] Département des Sciences de la Terre et de l'Atmosphère, Université du Québec à Montréal (UQÀM), Montréal, QC H3C 3P8, Canada

[4] Coopérative de Solidarité GÉOCOOP, Montréal, QC H1K 5G6, Canada